Geosciences

AIMS Geosciences, 12(2): 388–422.
DOI: 10.3934/geosci.2026015
Received: 16 October 2025
Revised: 27 January 2026
Accepted: 02 March 2026
Published: 03 April 2026

https://www.aimspress.com/journal/geosciences

Research article

Fluxing with CO_2 of rhyolitic magma at the beginning of an eruption—scholastic concept or reality?

Alexander G Simakin* and Vera N Devyatova

Institute of Experimental Mineralogy RAS, Chernogolovka, Moscow region, Russia

* **Correspondence:** Email: simakin@iem.ac.ru; Tel: 007(495)5225853.

Abstract: The volumes of CO_2 released at some basaltic volcanoes (e.g., Etna, Stromboli) significantly exceed the limits of solubility in silicate melt, indicating flushing by deep, CO_2-rich fluids from crustal and mantle sources. A similar flushing mechanism in silicic magmatic systems has been less evident. Here, we propose that H_2O–CO_2 contents in quartz-hosted melt inclusions (MIs) can serve as an indicator of interaction between hydrous rhyolitic magma and carbonic fluid. Numerical modeling of this interaction process at the single-bubble scale, accounting for volatile diffusivity dependencies on water content, demonstrates that a uniformly dehydrated melt with highly variable CO_2 concentrations can form on relatively short timescales. In natural magma bodies where bubble coalescence and escape occur, this process generates melt compositions that form subvertical arrays on H_2O–CO_2 diagrams. Such compositions, preserved in melt inclusions, are commonly found in pyroclastic deposits from catastrophic intraplate rhyolitic eruptions, such as those of the Yellowstone caldera. Reinterpretation of extensive published MI data from the pre-Huckleberry Ridge Tuff-A ashfall deposits at Yellowstone reveals episodes of carbonic fluid-magma interaction that likely initiated explosive eruptions. The first eruptive cycle is associated with flushing at the basal boundary layer of the magma chamber by a fluid enriched in CO_2 and Li. The resulting bubbly layer would ascend rapidly, being captured in the earliest erupted magma that forms the base of the ash sequence. MIs from this level show a strong positive correlation between CO_2 and Li concentrations. In contrast, a significant negative correlation between CO_2 and Li is observed in MIs from near the top of the 2-meter-thick ash sequence. This pattern is attributed to a second, distinct flushing episode by a Li-poor fluid, which culminated in the massive early Huckleberry

Ridge Tuff (HRT-A) ignimbrite eruption that overlies the ashfall deposits. Other samples exhibit a strong positive correlation between Li and H_2O, explainable by syneruptive diffusive loss of both components. Diffusive water loss from reentrants and MIs consistently indicates a syneruptive magma decompression rate of ~0.02–0.06 MPa/s. Finally, the unusual population of reentrants and MIs with uniformly low H_2O (1–1.5 wt.%) but variable-to-high CO_2 contents at the top of the ash section can be explained by dehydration during interaction with (or formation from) a water-poor melt. This melt was likely generated by remelting of largely solidified rhyolite, underplated by basalt, as an alternative or complementary process to CO_2 flushing.

Keywords: rhyolitic eruption; melt inclusion; vesiculation; CO_2 fluxing; diffusion chronology; reentrants

1. Introduction

The transition of magma to a two-phase state with fluid bubbles at a storage depth has a strong effect on its physical properties: density and compressibility and on the mechanical state of the magma chamber. According to estimates [1], intrachamber vesiculation leads to an increase in the duration and volume of erupted magma up to 30 times compared to the eruption of magma undersaturated with volatile components. Saturation with volatile components can be achieved not only by crystallization [1] but also by the influx of CO_2 from below even into a melt that is undersaturated with water since the solubility of water decreases with increasing molar fraction of CO_2 in the fluid. At a sufficiently high fraction of CO_2, melt dehydration and an increase in the volume of fluid phase bubbles occur [2].

The process of gas bubbles rising through two liquid layers from below was experimentally studied by Thomas et al. [3]. They observed the formation of rising convective plumes of bubbly liquid when the upper layer had a higher viscosity, which resulted in the accumulation of bubbles in it. As follows from the theoretical analysis, the liquid layer with bubbles emerging from the lower boundary exhibits Rayleigh-Taylor instability at the sedimentation Rayleigh number (Ra_s):

$$Ra_s = \frac{(\rho_l - \rho_{fl})\varepsilon_{fl} g H^2}{S\mu} \tag{1}$$

Ra_S greater than 105 [4]. Here, r_l and r_{fl} are the densities of the melt and bubbles, respectively; e_{fl} is the volume fraction of the bubbles; m is dynamic viscosity of the melt; S is the Stokes velocity of bubble ascent; and H is the thickness of the magma layer (chamber thickness). This condition is almost always satisfied at the parameters characteristic of rhyolite magma. The characteristic convection velocity and overturn timescale are given by [4]:

$$U_{conv} \approx S\sqrt{Ra_s/8}\,, \qquad t_{conv} = H/U_{conv} \tag{2}$$

where S is the Stokes settling velocity for a bubble of radius R. Using standard values ($H = 1000$ m, $\mu = 10^5$ Pa·s, $g = 9.8$ m/s^2, $\rho_l = 2300$ kg/m^3, $\rho_{fl} = 500$ kg/m^3) and a bubble radius $R = 1$ mm, we calculate t_{conv} to be 2–3 days for fluid volume fractions of 0.03 and 0.01.

With sufficient vertical extension, the rise of magma with bubbles is accompanied by expansion of the fluid and a significant increase in pressure in the chamber, which was first proposed in [5]. The triggering of volcanic eruptions by distant earthquakes can sometimes be explained by this effect of advective overpressure associated with the rise of bubbles [6]. Accurate calculation of magma pressure in the chamber requires taking into account the increase in its volume, magma compressibility [7], and the solubility of the two-component fluid in the melt with increasing pressure [8]. Crystallization of the melt due to dehydration caused by CO_2 fluxing heats the magma and also leads to the release of additional fluid [9]. Thus, intra-chamber bubbling at the bottom from CO_2 fluxing can potentially cause an eruption.

Many active magmatic silicic systems, such as Yellowstone and Bishop Tuff, have high observed CO_2 fluid fluxes at the surface. This fluid of deep lithospheric or mantle origin is transported to the surface, is dissolved or dispersed in basaltic magma or as a separate phase, and can provide fluxing of underplated silicic magma. This hypothesis is supported by data from [10], who found fluid-filled reentrances (or embayments) in about half of quartz phenocrysts from LCT (Yellowstone). Some of such reentrances were later filled with melt. Similar evidence of magmatic quartz growth surrounded by fluid bubbles, which may be caused by CO_2 invasion, has been reported in the Toba Tuff (Indonesia) and Oruanui Tuff (New Zealand) (see references in [10]).

Much attention has recently been paid to the study of the volatile content of melt inclusions and embayments in quartz from the products of explosive silicic eruptions. Based on these data, it is possible to distinguish between the manifestations of normal decompression degassing of magma during an eruption and intra-chamber degassing caused by CO_2 fluxing. To do this, it is necessary to recognize the signs of various factors, including a significantly lower diffusion rate of CO_2 in the melt compared to water. At certain time scale, this leads to rapid dehydration while maintaining the CO_2 content during both decompression and CO_2 fluxing-induced degassing.

The interaction of carbonaceous fluid and hydrous silicic melt was experimentally studied by Yoshimura and Nakamura [11] and Simakin et al. [9]. Both studies showed that the melt layer dehydrates faster than CO_2 is diffusively transferred from the fluid into the melt. Simakin et al. [9] used a starting glass powder with CO_2-filled pores that transformed into a bubbly melt upon heating. The initial volume fraction of bubbles was about 40 vol.%, and over time, the bubbles escaped from the melt. This run setting ensures rapid (within minutes) uneven dehydration and saturation with CO_2: some portions of the melt reach equilibrium composition, while others are predominantly dehydrated.

Yoshimura and Nakamura [12,13] attempted to apply their experimental results to theoretical modeling of CO_2 fluxing of basaltic magma in extended vertical volcanic conduit in relation to the volcanoes Etna and Stromboli. Yoshimura and Nakamura [12] modeled vertical fluid flows rather arbitrarily as ascending jets of bubbles or through a network of interconnected pores crossing the melt and absorbing water from it in a one-dimensional diffusion approximation. Yoshimura and Nakamura [13] used an equilibrium approximation of this problem, since for channel lengths of km-tens of km, on times of months-years, diffusion effects are not significant. Simakin et al. [9]

performed numerical simulations of CO_2 fluxing using an assemblage of uniformly sized bubbles, including the effect of melt flow around growing bubbles on the diffusion transport of volatiles in the melt. Our approach is aimed at describing the processes of CO_2-melt interaction on short time scales of the order of up to hours in a convective boundary layer of about a meter in thickness. For such parameter values, the Stokes bubble rise time scale and local diffusion time scale are close. Both experimental and theoretical results of different authors confirm that during CO_2 fluxing, one can expect a specific character of change in the content of H_2O and CO_2 in the magmatic melt preserved in melt inclusions and embayments in quartz.

Interpretation of data on the content of volatile components in melt inclusions in quartz is complicated by their possible loss during and after the eruption. In the experimental study of the preservation of melt inclusions in quartz during long-term exposure to magmatic PT parameters Severs et al. [14] observed water concentration decrease from 5.5 to 2 wt.% in 5 days. The results of this study had not been sufficiently processed; strictly speaking, it remains unclear to what extent and how they are applicable when working with MIs in quartz from climatic silicic eruptions.

In this paper, we present improved results of numerical modeling of silicic melt fluxing by carbon dioxide fluid [9] at the micro level accounting for the dependence of the diffusion coefficients of volatile components on the water content. This allowed us to clarify the time of initial uniform dehydration depending on the initial bubble size and the volume fraction of the fluid phase. Equations for the analysis of diffusion mass transfer in embayments and inclusions in quartz, both under experimental and natural conditions, were also analyzed and refined. Profound analysis of published data on the contents of CO_2, H_2O, and lithium in embayments and inclusions in quartz of pyroclastic rocks from the initial stage of the Yellowstone HRT eruption [15] made it possible to identify signs of magma fluxing by juvenile CO_2 at the initial stage of the eruption. Also, distinct traces of interaction between the roof melt and CO_2-enriched fluid exsolved from rhyolite magma at depth during the eruption were revealed.

2. Diffusion control of the trajectory of H_2O-CO_2 contents in the melt during flushing by carbonic fluid

2.1. Model

In our previous publication [9], for simplicity, we considered the dehydration of rhyolitic magma by a carbonic fluid by assuming constant diffusion coefficients of H_2O and CO_2, which allowed the use of linear moving-grid partial differentiation equations methods. However, the diffusion coefficient of water depends on the water concentration. Molecular water diffuses faster in the melt than hydroxyl, which predominates at low total water contents of less than about 2–2.5 wt%. The diffusion rate of CO_2 also decreases toward drier, more viscous compositions. To simulate the interaction of CO_2 bubbles with a hydrous melt taking into account the variable diffusion coefficients of water and CO_2, we used the numerical control volume method to discretize Eqn. 3 of diffusion in the spherical shell approximation (see the implementation in [16]):

$$\frac{\partial C_i}{\partial t} = -U(r)\frac{\partial C_i}{\partial r} + \frac{\partial}{\partial r}\left(\frac{1}{r^2}D(\bar{C})\frac{\partial C_i}{\partial r}\right), \qquad i = H_2O, CO_2 \tag{3}$$

where diffusion coefficient (*D*) in general depends on the concentrations of both components (vector *C*). In this approximation, the vesiculated volume is represented as a set of identical bubbles of radius $R_0(t)$ inside a spherical shell with an outer radius $R_1(t)$ and a radial coordinate *r*. The volume of the shell does not change during the growth (dissolution) of the bubble; therefore, the radial velocity $U(r)$ decreases outward as $U(r) = U_b R_0^2/r^2$, where $U_b = U(R_0)$ is the radial velocity of the bubble wall. The volume of the bubble varies according to the variable mass and density of the fluid [17] calculated from the mass balance equation:

$$\frac{dm_{fl}}{dt} = \sum_i 4\pi\rho_m R_0^2 D_i \frac{\partial C_i}{\partial r}, \qquad i = H_2O, CO_2 \tag{4}$$

where m_{fl} is mass of fluid in the bubble, R_0 is radius of the buuble, and ρ_m is density of the melt. The positions of the radial grid nodes are shifted at each time step. At the bubble interface ($r = R_0$), the concentrations of water and CO_2 in the melt are calculated as their solubilities for the current fluid composition:

$$C_{H2O,m}=F_1(X_{CO2},P,T),\ C_{CO2,m}=F_2(X_{CO2},P,T), \tag{5}$$

where X_{CO2} is mole fraction of CO_2 in the fluid. We use the approximation of CO_2 and H_2O solubility for rhyolite melt from [9]. The outer boundary (at $r = R_1$) is assumed to be symmetrical (the boundary with other bubbles). The initial volatile content distributions are assumed to be $C_{CO2,0}(r) = 0$ and $C_{H2O,0}(r) = 5$. To avoid extremely high gradients in the first time steps, the initial distributions are smoothed at several grid nodes from a constant value to the equilibrium value. An explicit solution scheme with a time step satisfying the Newman-type stability condition is used.

The diffusion mobility of volatile components in magmatic melts has not been studied experimentally in detail. There is quite a large discrepancy typically of 0.5 log.units (3 times) between empirical models and measurements from specific studies. We selected an empirical formula for water diffusion [18] based on experimental data for haplogranite melt obtained over a wide range of parameters: $50 < P < 500$ MPa, $800 < T < 1200$ °C, $0.5 < C_w < 6$ wt.%. It predicts D_{H2O} values for PT parameters typical of crustal rhyolitic magma chambers beneath volcanoes that are systematically higher than those predicted by the model Zhang and Ni [19].

Zhang and Ni [19] proposed an expression for the diffusion coefficient of CO_2 in all magmatic melts as a function of pressure, temperature, and water content. It predicts values at water content 2–5 wt.% and P = 200 MPa higher than approximation of experimental data for rhyolitic melt from [20] on 0.3–0.4 log units. The model of Zhang and Ni [19] predicts a D_{CO2} value at 4 wt% water content, T = 1020°C and P = 200 MPa of 1.5e–11 m^2/s, exactly the same as the value we measured under these conditions in albite melt [9].

In the context of melt fluxing with carbon dioxide fluid, the value of the D_{CO2}/D_{H2O} ratio is significant. Due to the inconsistency of experimental data, we can combine different data sources for

CO_2 and H_2O. Combining [20] for CO_2 and [19] for H_2O gives an average value of $r_D = D_{CO2}/D_{H2O}$ of 0.14 (T = 900°C, P = 200 MPa, C_{H2O} in the range 2–4 wt.%). At the same time, taking the review [19] as a data source for both CO_2 and H_2O gives an average value of r_D of 0.29 (C_{H2O} in the range of 2–4 wt.%) with a maximum value of $r_D(C_{H2O} = 5$ wt.%$) = 0.78$. In this case, at high water content, the diffusion coefficient of CO_2 is almost equal to the diffusion coefficient of H_2O, which contradicts the experimental data.

For the following calculations, we employed the model of Zhang and Ni [19] for CO_2 diffusion coefficients and that of Novak and Behrens [18] for H_2O diffusion coefficients. Consequently, the ratio of diffusion coefficients, $r_D = D_{CO2}/D_{H2O}$, depends on both water content and temperature. For the water concentration interval of 1.5–5 wt.%, the average values of r_D are $r_D(T = 800^oC) = 0.071$, $r_D(850^oC) = 0.104$, and $r_D(900^oC) = 0.204$. The diffusion equations were scaled using the diffusion coefficient for water, $D_{w,0}(T_0,P_0,C_{w,0})$, at pressure P_0 = 200 MPa and an initial water concentration $C_{w,0}$ = 5 wt.% for a given temperature T_0. The length scale for the spherical shell problem is the initial bubble radius R_0, which defines the corresponding diffusion time scale $t_0 = R_0^2/D_{w,0}$. Initial mole fraction of CO_2 in the fluid was $X_{CO2} = 0.8$.

2.2. Results of numerical modeling

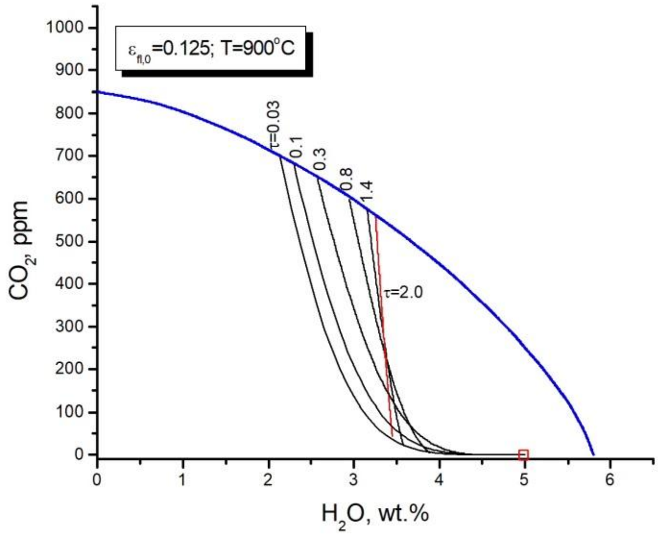

Figure 1. Results of numerical simulation of diffusion exchange between a CO_2 fluid bubble and an hydrous silicious melt, with H_2O and CO_2 diffusion coefficients dependent on the water content. The initial mole fraction of CO_2 in the liquid is 0.8; the pressure is P = 200 MPa; and the initial water content in the melt, 5 wt.%, is indicated by a square. Projections of the radial distributions of CO_2(r) and H_2O(r) are plotted, indicating the corresponding dimensionless times near the curves.

The results of the numerical modeling are presented in Figure 1, which plots melt composition in C_{H2O}–C_{CO2} coordinates, analogous to common representations of melt inclusion data. The boundary melt compositions correspond to equilibrium with the fluid at the bubble interface and the symmetry boundary, respectively. All modeled compositional profiles exhibit a concave shape. The progressive enrichment of the bubble in H_2O is reflected in a shift of the melt composition along the solubility curve toward the H_2O apex. Over time, the water concentration in the melt shell approaches a uniform distribution, whereas the CO_2 concentration remains far from equilibrium.

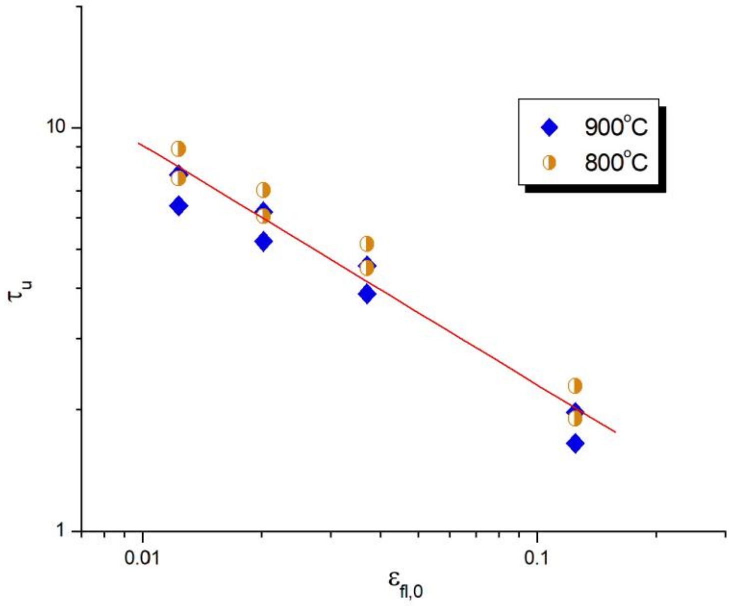

Figure 2. Dependence of the normalized time for reaching the uniform water distribution around carbonic fluid bubble (τ_u) during the diffusional exchange with hydrous melt as a function of the initial fluid volume fraction. Upper and lower values of τ_u at given temperature calculated for values of water concentration contrast in the melt of 0.2 and 0.3 wt.%, respectively. Initial mole fraction of CO_2 (X_{CO2}) was 0.8.

We define the time to reach a uniform water distribution, τ_u, as the time required for the difference between the boundary concentrations to decrease to 0.2–0.3 wt.% (a value close to the typical analytical uncertainty for H_2O determination). We calculated τ_u at T = 800ºC and 900 ºC for various values of R_1 and corresponding initial volume fraction of fluid $\varepsilon_{fl} = (R_0/(R_0 + R_1))^3$ (see Figure 2). The data show no significant difference between the two temperatures. Combined, numerical data for both temperature series are well approximated by a power-law dependence. The linear approximation in logarithmic form is:

$$\log(\tau_u) = -0.231 + 1.782 \log\left(\frac{\mathrm{R}_1}{\mathrm{R}_0}\right) = -0.231 + 1.782 \log\left(\frac{1}{\varepsilon_{fl}}\right)/3, \quad (6)$$

with a standard deviation (1σ) of 0.056.

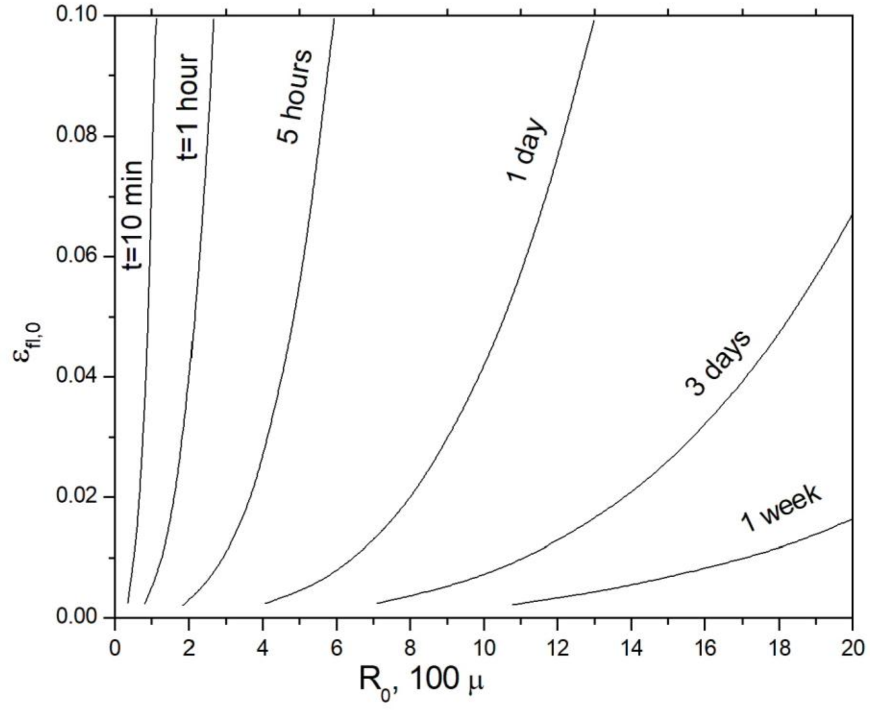

Figure 3. Numerical estimate of the minimum time (τ_u) required to achieve a uniform H_2O distribution in a bubble-bearing melt, as a function of initial bubble radius (R_0) and initial fluid volume fraction ($\varepsilon_{fl,0}$). The model assumes an initial CO_2 mole fraction in the fluid of X_{CO2} = 0.8 and an initial H_2O concentration in the melt of $C_{w,0}$ = 5 wt.%. Results are valid for the temperature range of 800–900 °C.

In Figure 3, the time to achieve uniform water distribution (calculated using Equation 6) is plotted as a function of both the bubble volume fraction and the initial bubble radius R_0 (expressed in units of 100 μm). Experimental conditions are typically characterized by small bubbles (R_0 = 20–50 μm), for which τ_u is on the order of only a few minutes (see Figure 3). This result is consistent with experimental observations. For instance, Yoshimura [21] measured radial compositional gradients around bubbles in a rhyolitic melt after interaction with an external CO_2–H_2O fluid. In experiments lasting approximately one hour, they found significant CO_2 gradients but a nearly uniform H_2O distribution, in full agreement with our analysis. Scaling our model to larger bubbles and lower volumetric fractions typical of magma chambers, we obtain estimates for τ_u ranging from approximately one hour to one week.

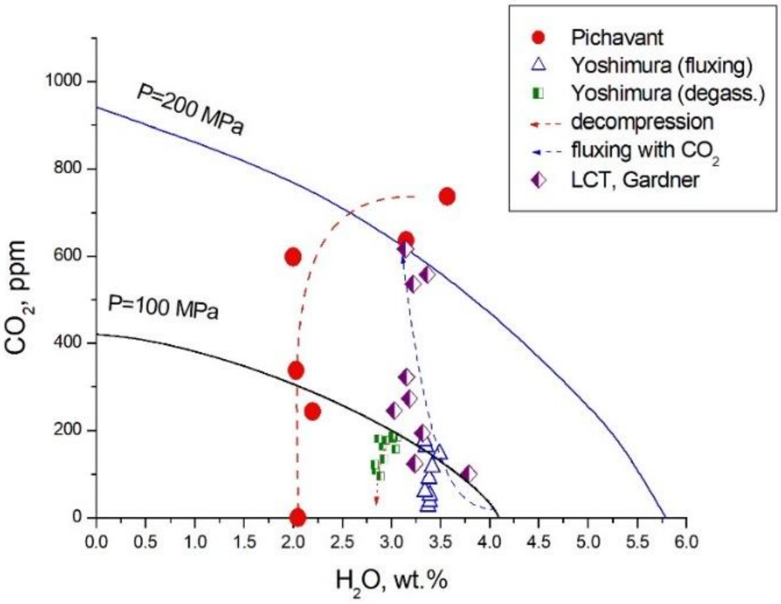

Figure 4. Trajectories of disequilibrium flushing and degassing processes in the melt-CO_2-H_2O system, which are projections of the concentration distributions in the melt $C_{H2O}(z)$ and $C_{CO2}(z)$, where z is the distance from the interface (meniscus or bubble boundary). Decompression degassing ([22] and [11]) produces a clockwise-rotated (CO_2 exsolved first) trajectory during equilibrium degassing and a counterclockwise-rotated (H_2O first) trajectory during disequilibrium degassing. Flushing by carbon dioxide fluid produces a clockwise-rotated trajectory evolving toward a vertical line with time. Melt inclusions in quartz from the Yellowstone LCT climatic eruption data [23] are plotted for comparison.

2.3. *Diffusional control in experimental data*

The slower diffusion of CO_2 in the melt than water on the corresponding time scale is expressed in decompression degassing of magma, as well as in the CO_2 flushing discussed above. Water is lost first, not simultaneously CO_2 and H_2O, as in equilibrium close (and open) system degassing, forming inclined trajectories on volatiles contents diagram. This process has been observed experimentally in a one-dimensional setting (bulk degassing from the surface) [22] and around individual bubbles [21]. The results of these studies are shown in Figure 4. Pichavant et al. [22] captured an intermediate state before complete melt homogenization with water. The distribution of CO_2 and H_2O at the contact with the carbon dioxide fluid (a one-dimensional analogue of CO_2 flushing) from [11] is also displayed in Figure 4. Both nonequilibrium degassing and flushing lead to a subvertical distribution of melt compositions in the H_2O-CO_2 diagram. They differ in their starting points and at times smaller than τ_u.

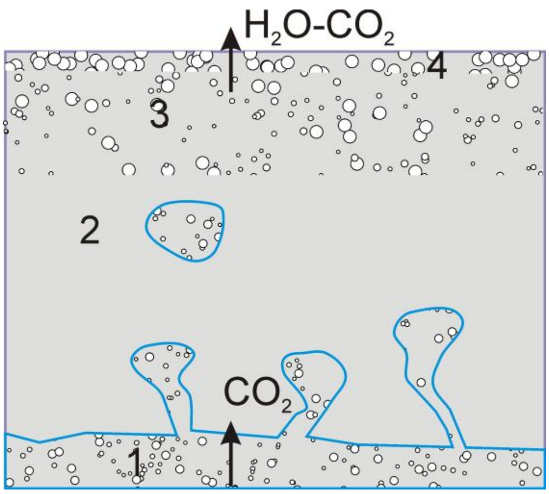

Figure 5. Schematic illustration of two-phase convection in a magma chamber due to fluid inflow from the bottom. Rising bubbles form a gravitationaly unstable two-phase boundary layer. At continuous flushing with time, stratification in the magma layer develops, including 1) lower zone of active magma-fluid interaction producing periodic bubbly magma plumes, 2) zone of the clean magma periodically intersected by plumes, 3) zone of accumulated two-phase magma where bubbles coalesce and rise to immediate contact with roof rocks, and 4) magma in zone 3 contains uncoalesced tiny bubbles.

Both degassing and flushing cause melt dehydration and thus an increase in the liquidus temperature of magmatic minerals and their crystallization [9]. Growing at large undercooling minerals have a kinked habit and capture melt inclusions that record the content of volatile components. Distributions of MI compositions in quartz from climatic rhyolitic explosive eruptions with respect to H_2O and CO_2 contents sometimes form a subvertical sequence, as can be seen in Figure 4 from the Lava Creek Tuff eruption data [23]. During the flushing process, a vertical array of melt inclusion composition points would form on a H_2O-CO_2 diagram if bubbles escape from their host melts at varying degrees of CO_2 saturation. In this case, the decrease in water content from its initial value would correspond to the characteristic bubbles volume fraction (ε_{fl}), while the CO_2 concentration would range from the saturation value at a given X_{CO2} (established during the dehydration stage) down to the initial CO_2 content of the melt (see Figure 1).

Additional information is needed to interpret vertical distribution and attribute it to a degassing or flushing process.

2.4. *When diffusion control can be important in nature*

The effect of CO_2 and H_2O decoupling due to diffusion in the melt during flushing or degassing is important when the characteristic time of the process under consideration is compatible (close) to τ_u. According to [21], the flow time of magma rising in a conduit during an eruption, $\tau_{flow} = H/u_{flow}$ (here, H is conduit length, u_{flow}—flow velocity), satisfies this condition $\tau_{flow} \div \tau_u$ when the flow velocity approaches approximately 25–50 m/s (pressure drop rate 0.7–1.4 MPa/s), which corresponds to τ_{flow} = 5–10 min at H = 10–15 km (mid-crustal magma chamber). For high bubble volume fraction and low viscosity basaltic magma this is a reasonable time value. The calculated depressurization rate is between estimates based on MI data in olivine [24]: 0.1–2 MPa/s for the 2017–2018 Plinian eruptions of Ambae volcano and 0.4 MPa/s for the 1650 sub-Plinian eruptions of Kilauea volcano.

In the following, we consider the effects of disequilibrium flushing of the rhyolitic magma chamber with CO_2 fluid as a trigger for explosive eruption. In this case, the bubbles interact with the magma for a time proportional to the Stokes time of bubbles rising in the lower boundary layer in compositional two-phase convection (see Figure 5). The thickness scale of the viscous boundary layer in a rhyolitic magma chamber in two-phase convection is 1 m [25]. Accordingly, the Stokes time becomes compatible with τ_u for sufficiently large coalesced bubbles of 1–2 mm in diameter depending on the melt viscosity [9].

3. The problem of conservation of volatiles in MIs in quartz after an eruption

MIs in minerals carry information about the content of volatiles at different stages of magma volume evolution before and during the eruption (e.g., [26]). Based on the pattern of MIs in olivine composition distribution on the H_2O-CO_2 diagram, the mechanism of slow (lasting several years) equilibrium flushing of basaltic magma of Etna and Stromboli with CO_2 before the eruption in a volcanic conduit up to 15 km long is suggested [13]. Considering almost the same data for Etna, Yoshimura [21] tried to recognize signs of disequilibrium degassing (exsolution of H_2O before CO_2) of basaltic magma rising during the eruption at different rates. However, it has recently become clear that at high temperature MIs can rapidly exchange H_2O with the environment (atmosphere or host magma). Therefore, MIs data, especially for olivine [24], can be used with caution and, as a rule, require correction.

3.1. Interpretation of experimental data on the water loss from MIs in quartz

Although quartz is a more durable host for MIs than olivine and inhibits volatile loss more effectively, water can still diffuse from MIs in quartz on a timescale of days to weeks at high temperatures. This is demonstrated by the experiments of Severs et al. [14], who subjected MIs in natural quartz to 800 °C and 100 MPa. Their results show a drop in water content from 5.3 to 2 wt.% over roughly one week.

Experimental data [14] show that melt inclusions lose 0.5 wt.% of their water content within the first four hours, at a rate far exceeding that observed over the next 100–1000 hours. This initial, rapid dehydration is likely driven by hydrogen diffusion through quartz, where the hydrogen is produced by water decomposition. The concurrent oxidation of ferrous iron in the melt consumes the liberated oxygen, as described by the reaction:

$$Fe^{2+} + 1/2H_2O = Fe^{3+} + 1/2H_2 + 1/2O^{2-} \qquad (7)$$

Achieving this 0.5 wt.% water loss via hydrogen diffusion requires the melt to contain ~1 wt.% FeO. Subsequently, the dehydration rate becomes limited by the diffusion of water itself within the quartz.

The problem of water loss from a melt inclusion in quartz can also be solved using the spherical shell approximation. In this case, R_0 is the radius of the melt inclusion and R_1 is the radius of the isotropic spherical shell representing the quartz crystal hosting it. The radius R_1 can be interpreted as the characteristic distance from the surface of MI to the surface of the quartz crystal.

The simplest analytical estimate of the rate of water loss from a melt inclusion can be obtained using a water mass balance:

$$\frac{dC_m(t)}{dt}\left(\frac{4\pi R_0^3}{3}\rho_m\right) = 4\,\pi R_0^2 q_{ss}(t)\rho_s, \tag{8}$$

where C_m is the water concentration in the MI and q_{ss} is the steady-state approximation of the diffusion flux of water in quartz at the boundary with the melt. It is easy to find the quasi-steady-state (slowly changing) concentration radial distribution $C(r)$ for given boundary concentrations $C_0 = C(r = R_0,t)$ and $C_1 = C(r = R_1,t)$. Suppose that in quartz at the boundary with the melt, the equilibrium concentration $C_m(t)$ is proportional to the concentration in the melt, $C_0 = k_D C_m(t)$, and at the outer boundary $C_1 = 0$. Then, the steady-state flux is equal to:

$$q_{ss} = D\frac{\partial C_{ss}}{\partial R} = -Dk_D\frac{C_m(t)}{R_0}\frac{b}{b-1}, \tag{9}$$

where $b = R_1/R_0$. After substituting the expression for q_{ss} (9) into Equation (8), we obtain a simple exponential solution of Equation (8):

$$C_m(\tau) = C_{m,0}\exp(-t/\beta\tau_0), \tag{10}$$

where $\beta = \frac{1}{3k_D}\frac{\rho_m}{\rho_s}\frac{b-1}{b}$ and time is scaled in units of $\tau_0 = R_0^2/D$. Indeed, for real MIs b >> 1 $\beta \approx \frac{1}{3k_D}\frac{\rho_s}{\rho_m}$; therefore, the coefficient β does not depend on the distance from MI to the edge of the crystal. Using a numerical solution, which is not presented here for brevity, it was shown that the analytical estimate is accurate to within 6–7% relative. In view of the approximate representation of experimental data on the geometry of the MIs by a spherical shell model with one parameter b, the analytical solution seems adequate for estimating the diffusion coefficient of water in quartz based on experimental data. Hentz et al. [27] reported a k_D value of 1.5e–04 as the most likely for quartz from silicic explosive eruptions, translating 5 wt% water in MI to 7.5 ppm in quartz. The density of the melt and quartz of 2.23 and 2.65 g/cm^3 are taken, respectively.

In the time interval 10–160 hours, the experimental data are well fitted with the exponential decay function (Eqn. 10) with $t_1 = \beta\tau_0 = 64$ hours. With the material parameters adopted above and radius of MI of 10 and 15μ (the range characterizing the size of MIs in [14]), we obtain the values of the water diffusion coefficient log(D) = −9.94 and −9.34 m^2/s, respectively. These estimates are in good agreement with the values reported by Kats [28] (see Figure 6) and are somewhat lower than the Li$^+$-H$^+$ diffusion exchange rate measured by Jollands et al. [29].

The most comprehensive study of water diffusion in synthetic quartz was conducted by Bachheimer [30]. The quartz used in that study was highly anisotropic, having been grown on a seed crystal, which resulted in an inherited array of parallel dislocations originating from the seed surface. His measurements for Z-sections perpendicular to the c-axis are almost identical to our estimates based on Severs et al. [14] data. For other sections of quartz crystals, the diffusion coefficients are several times lower. Moreover, ideal natural crystals with a low dislocation density have a 100-fold lower diffusion coefficient of water, which emphasizes the role of dislocations in H_2O transport.

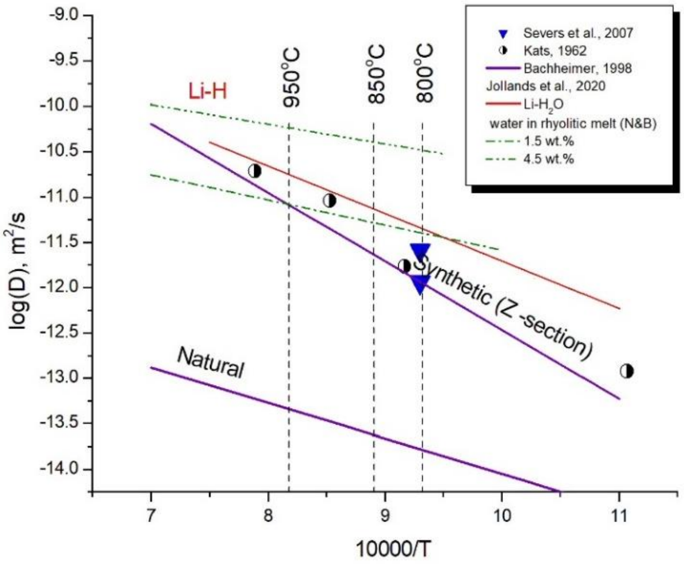

Figure 6. Experimental data on the diffusion mobility of water in quartz: the annealing method at atmospheric pressure was used by Katz [28] and Bachheimer [30]. The annealing method under conditions of diffusional supply of Li^+, compensating for diffusional losses of H^+, was used by Jollands et al. [29]. Our estimate is obtained from the data of Severs et al. [14] on water loss from MIs in quartz annealed at elevated pressure; inclusion sizes of 20 and 30 μm were used for smaller and larger values, respectively. For comparison, graphs of water diffusion coefficients in a silicic melt [18] with a water content of 1.5 and 4 wt.% were plotted.

For comparison, Figure 6 also shows graphs of changes in water diffusion coefficients in rhyolite melt with temperature at water content of 1.5 and 4 wt.%. In the temperature range of 800−950 °C and at a lower water content, the diffusion coefficients in quartz and melt are quite close, which reflects a similar mechanism of diffusion of water present in the form of OH groups in both cases. Indeed, the H^+ for Li^+ exchange mechanism for water diffusion in quartz proposed in [29] cannot be universally applicable. Cation exchange was not involved in the experiments of Kats [28] and Bachheimer [30], which yielded virtually identical diffusion coefficient values. The low mass rate of diffusion transfer of H_2O in quartz is due not to the slow diffusion of water but to its significantly lower content than in the melt.

3.2. *Nonlinear effects of volatile diffusion in melt reentrants in minerals*

Diffusion in the melt of embayments can be modeled to a first approximation in 1-D:

$$\frac{\partial C_i}{\partial t} = \frac{\partial}{\partial z}\left(D(\bar{C})\frac{\partial C_i}{\partial z}\right), \qquad i = H_2O, CO_2 \tag{11}$$

The diffusion coefficients of volatile components (CO_2, H_2O) in the melt depend significantly on the water content. This makes the diffusion problem nonlinear. We numerically modeled diffusion on an interval with a closed end ($\partial C/\partial z|_{z=L} = 0$) and a time-dependent concentration at the open end ($C(z)|_{z=0} = f(t)$).

The equation was transformed to a dimensionless form with a linear scale equal to the interval length L ($\zeta = z/L$) and time with a diffusion scale $t_0 = L^2/D(C_{H2O} = C_{H2O,0})$ $(\tau = t/t_0)$ and solved numerically using the Maple symbol manipulator (version 9.5). At small times, when the diffusion front has not reached the closed end, the solutions exhibit a self-similarity property. Specifically, solutions for given initial and boundary conditions at variable times have the same form depending on the parameter $\xi = \zeta/\tau^{1/2}$. This property is illustrated in Figure 7.

Three variants of the dependence of the boundary water concentration at z = 0 (embayment entrance) on time $C_b(t)$ were used. The constant value of C_b corresponds to an instantaneous decrease in the water content at t=0 (asymptotic limit of fast degassing). Regimes 1 and 2 of continuous degassing (Figure 7a) correspond to a concave (faster) and convex (slower) deviation from the linear dependence (see Figure 7a). In the first regime, the boundary concentration is taken as $C_b(t) = C_0-(C_0-C_{b,end})(t/\tau)^{1/2}$. The second regime is formulated to correspond to a constant rate of pressure drop and the dependence of water solubility on the square root of pressure: $C_b(t) = (C_0^2-(C_0^2-C_{b,end}^2)t/\tau)^{1/2}$. Figure 7b shows the graphs of solutions of the Eqn. 11 for water diffusion in rhyolite melt for numerical experiments of varying duration. Parameters: T = 800 °C, initial concentration $C_{H2O,0}$ = 3 and 5 wt.%, boundary concentration depends on time at different modes and with varying rates, the total numerical run time ranges from $\tau = 0.005$ to 0.1. When expressed through the dimensionless variable $\zeta/\tau^{1/2}$, all data for a specific variant are reduced to one curve.

The self-similar solution ($erfc(x/L/\tau^{1/2})$) for a problem with a constant diffusion coefficient and constant C_b is well known and is also shown. The solutions for instantaneously established C_b (for (C_0,C_b) = (5,1) and (3,1)) also demonstrate self-similarity features at short times. The shapes of the distributions for time-dependent ($C_2(z)$) and constant ($C_1(z)$) boundary concentrations are similar. The dependences of both types can be brought closer together (see Figure 7c) by selectively increasing the time: $C_1(\zeta/(1.5\tau)^{1/2}) \approx C_2(\zeta/\tau^{1/2})$ for mode 1 and $C_1(\zeta/(3\tau)^{1/2}) \approx C_2(\zeta/\tau^{1/2})$ for mode 2 of degassing. In other words, the diffusion times during stepwise degassing are 1.5–3 times shorter than those during continuous degassing. This means that for small dimensionless times it is practically impossible to determine whether the observed diffusion profile was formed with a continuous or stepwise decrease in C_b.

A dimensionless time of 0.06 with a reentrant length of 100 μ, a temperature in the range of 750–850 °C and a water content of 2–5 wt.% corresponds to a physical time of 2–20 min. In the time interval $0.06 < \tau < 0.15$, the diffusion profiles at D = const converge to the asymptotic function $C^*_{norm}(\zeta)$, shown in Figure 7d. This curve was calculated using the Fourier series representation of the solution of the diffusion equations on an interval (see, e.g., [31]). For a concentration-dependent diffusion coefficient, with decreasing maximum concentration, the shape profiles gradually evolve to

$C^*_{norm}(\zeta)$. A shape close to asymptotic can correspond to a diffusion time of up to 5 days. The emergence of a well-defined asymptotic distribution in petrological practice can be illustrated (see Figure 7d). The distribution of CO_2 in the olivine embayment of Hawaiian volcanoes [32] show a distribution close to the asymptotic $C^*_{norm}(\zeta)$ law. This observation implies that at given PT conditions and low water content (<0.5 wt.%), the diffusion coefficient of CO_2 in basaltic melt is constant and CO_2 degassing takes a long time $\tau > 0.15$.

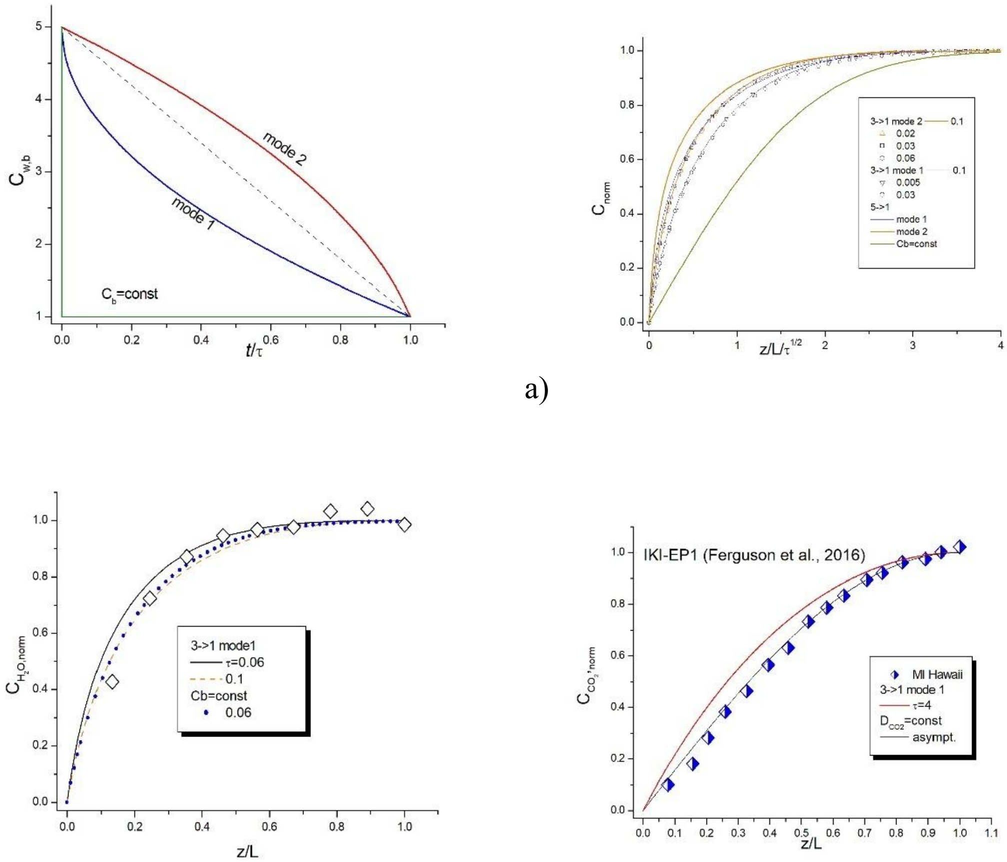

a) b)

c) d)

Figure 7. Concentration-dependent diffusion on the interval a) different variants of the time-dependent boundary condition $C_b(t)$ used in the calculations b) calculated shape of water diffusion profiles in the variable $x/L/\tau^{1/2}$ at short times for $C_{H2O,0}$ = 3 and 5 wt.% and C_b = 1 wt.%, time-dependent variants of $C_b(t)$ are indicated. For comparison, the self-similar solution ($erfc(x/L/\tau^{1/2})$) for the case of a constant diffusion coefficient is also shown c) instantaneous or continuous degassing (time-variable Cb) do not significantly affect the shape of the diffusion profile; The water concentrations in embayment from [33] are equally well approximated by the continuous mode 1 (τ= 0.1) and instantaneous degassing (τ= 0.06) profiles; d) the asymptotic shape of the long-time diffusion profile for a constant diffusion coefficient and for continuous mode 1 degassing ($C_{H2O,0}$ = 3 and C_b = 1 wt.); the embayment in olivine CO_2 distribution from [32] closely matches the asymptotic shape of the constant diffusion coefficient case.

3.3. Use of the maximum volatile content in reentrant for diffusional chronometry

Attempts to interpret distribution shape of a volatile component (CO_2 or H_2O) using a detailed scheme of degassing process (e.g., [34]) are subject to many uncertainties. Myers et al. [35] demonstrated that the differences in measurement results obtained using different methods can be significantly greater than, for example, the difference in the shape of distributions formed by instantaneous and continuous degassing shown above. Furthermore, a one-dimensional approach can be an oversimplification due to the influence of the three-dimensional shape of the embayments [36]. There are certain degassing styles (intrachamber flushing, disequilibrium, where water is released first) that are not accounted for in existing models. An additional complication is the secondary hydration of glasses, which distorts the shape of the distribution near the embayment entrance [37], reducing the informativeness of these data.

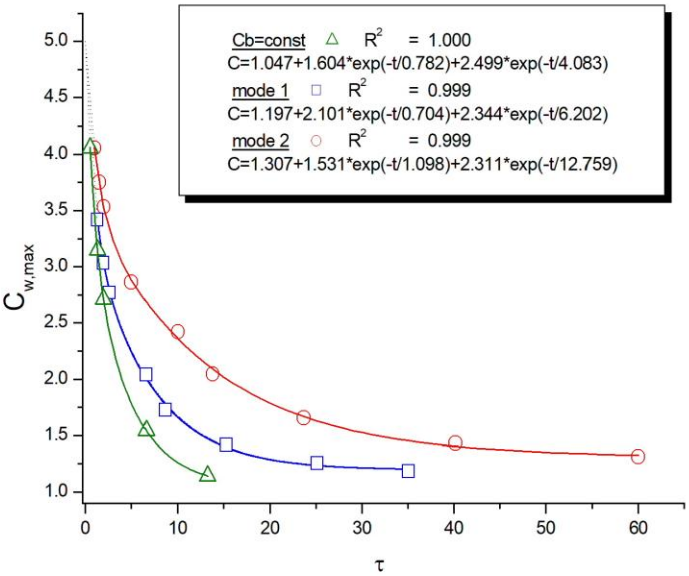

Figure 8. Approximation of numerical results for the decrease in the maximum water concentration with time for a concentration-dependent diffusion coefficient [18]. The calculations were performed using an initial uniform concentration on the interval $C_{H2O,0}$ = 5 wt.% and a final boundary concentration z = 0: $C_{b,end}$ = 1 wt.%. Different modes of dependence $C_b(t)$ corresponds to notations in Figure 7a.

Given these complexities, a viable method of interpretation may be to estimate the diffusion time required for the maximum concentration in the embayment at its closed end to decrease to the observed level. The maximum concentration decreases exponentially. In the case of a constant diffusion coefficient, exponential decay law is obeyed exactly. Using values calculated with analytical Forier series solution yields expression for τ > 0.2:

$$C_{max} = 1.273\, exp(-\tau/0.405) \tag{12}$$

This formula follows directly from the Fourier series solution (similar to the equation for diffusion in olivine [38]).

We numerically simulated water diffusion profiles over long timescales under various conditions and analyzed the rate of decrease in maximum values with time. The same $C_b(t)$ dependences as those described above for short timescales were used. Since diffusion transport slows over time, there is no single diffusion timescale. All three dependences for $C_{H2O,0}$ = 5 wt.% and C_b = 1 wt.% are well approximated by the sum of two exponentials (see Figure 8). The rate of concentration decrease at low concentrations is determined by the second exponential.

4. Analysis of MI and reentrants data on explosive eruption of rhyolitic magma in terms of the CO_2 fluxing concept

The concept of CO_2 flushing in rhyolitic eruptions can be tested based using recently accumulated extensive analytical data on the composition of melt inclusions and embayments in quartz [15,29,39]. The most detailed information on volatiles content was presented in the work of Myers et al. [15], who studied the ashfall deposits preceding Phase A of the Huckle Berry Tuff (HRT) Yellowstone eruption. Later, Swallow et al. [40] studied geochemistry and minerals composition of the same deposits and contacting ignimbrites. The HRT caldera-forming eruption at 2.08 Ma initiated the series of three major Yellowstone eruptions [40,41]. This eruption produced three ignimbrite members (A, B, and C) and two ashfall deposits: an initial pre-A fall deposit and another between members B and C. These ashfall deposits are presumed to correspond to explosive eruptions involving a layer of crystal-poor rhyolitic magma formed above zones of crystal mush and cumulates in a several thousand years before eruption [42]. Recalculated on the Ab-Or-Qz basis compositions of glasses of pre-HRT-A ashfall deposits (data source supplementary materials to [15]) are plotted in Figure 9. These compositions locate near cotectics of Ab-Or-Qz system at P_{H2O} = 100 and 200 MPa. Additional 2–3 wt.% of normative anorthite present in the considered glasses shifts cotectics minimum towards more Qz- and Or-rich compositions. Reducing of the water activity (reducing of mole fraction of H_2O in CO_2-H_2O fluid for fluid saturated magmas and reducing of H_2O content below saturation level for fluid-absent magmas) shifts position of minimum to more Or-rich composition [43] (see Figure 9). It is also worth noting that the agpaitic index (the atomic ratio [Na + K + 2Ca]/Al) of the glasses averages 1.06 ± 0.04, with maximum value of 1.22. This moderately increased alkalinity likely reflects magma-fluid interaction and could be attributed, for example, to the dissolution of $NaHCO_3$ transported by a fluid into the melt.

Swallow et al. [40] estimated feldspar-plagioclase equilibration temperatures. The dependence of the maximum temperature on depth within the studied ash sequence is plotted in Figure 10a, where the positions of samples from [15] are also marked. Maximum two-feldspar geothermometer temperatures for the ashes range from 800 to 860 °C, with an upper 1σ boundary at 910 °C. At the base of the HRT-A ignimbrite layer, temperatures increased to 980 °C (1σ boundary). The temperature profile exhibits two global minima, each followed by a rapid rise (see Figure 10a). One temperature cycle was initiated by an event at the time of the MM11 sample and another by an event corresponding to the YP287-MM3 samples. Within a single-magma-layer model, entrainment of the deepest magma is expected at a position corresponding to sample MM7, which exhibits the highest temperature and the lowest CO_2 content (see Table 1). The upper boundary layer with the lowest temperature and a local maximum in CO_2 content was sampled between the formation times of the MM10 and MM9 samples and at a later stage, near sample MM3. The first cycle produced the ashfall, and the second initiated the HRT-A ignimbrite eruption.

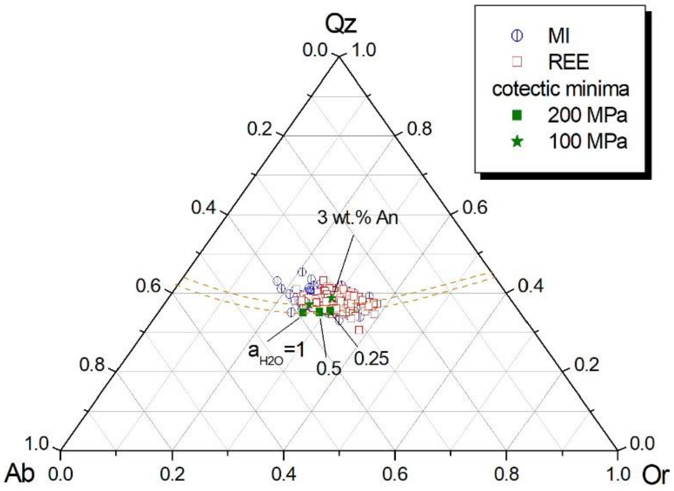

Figure 9. Composition of glass from MIs and reentrants (REE) in quartz phenocrysts from pre-HRT-A ashfall deposits, projected onto the Ab-Or-Qtz ternary diagram (data from [15], supplementary materials). Experimentally derived cotectics at 100 and 200 MPa H_2O pressure are shown as dashed lines. Stars indicate the positions of cotectic minima for a melt with 0 and 3 wt.% anorthite at P_{H2O} = 100 MPa and filled squares for a_{H2O} = 1.0, 0.5 and 0.25 at P = 200 MPa (data from [43]).

Swallow et al. [40] classified all glass shards and obsidian pyroclasts from the fall deposits into four clusters based on Ba and La concentrations, interpreting them as representing multiple, discrete melt-dominant domains tapped by separate vents. The Ba and La contents of glasses from [15] are plotted in Figure 10 b,c and classified into three clusters (our first cluster combines the two low-Ba clusters of Swallow et al. [40]). Barium concentration decreases during the fractional crystallization of feldspar (sanidine), whereas La content is primarily controlled by slow zircon dissolution, as feldspar temperatures generally exceed the maximum zircon saturation temperature of ~800 °C [40]. Thus, the first cluster represents the most fractionated magma and the second a less fractionated one. The third cluster may reflect an effect of cumulate melting by underplated basalts, potentially enhanced by fluid-mediated Ba transfer. Experimental data on the solubility of inorganic compounds in CO_2-rich fluids under high P–T conditions remain limited, with existing studies focusing primarily on systems, such as NaCl (e.g., [44]). However, studies of fluid inclusions in mantle xenoliths suggest that CO_2-dominated fluids in the upper mantle may exhibit significant solubility for certain trace elements, including LILE (e.g., Ba and LREE) [45]. Therefore, given the current state of research, rigorous validation of the fluid-transport hypothesis through detailed geochemical modeling is not yet possible. Accepting a single-magma-volume model, we conclude that during the eruption, the magma composition evolved, as samples MM11–MM7 in Figure 10 b,c fall mainly into cluster 1, while MM6–MM3 fall into clusters 2 and 3.

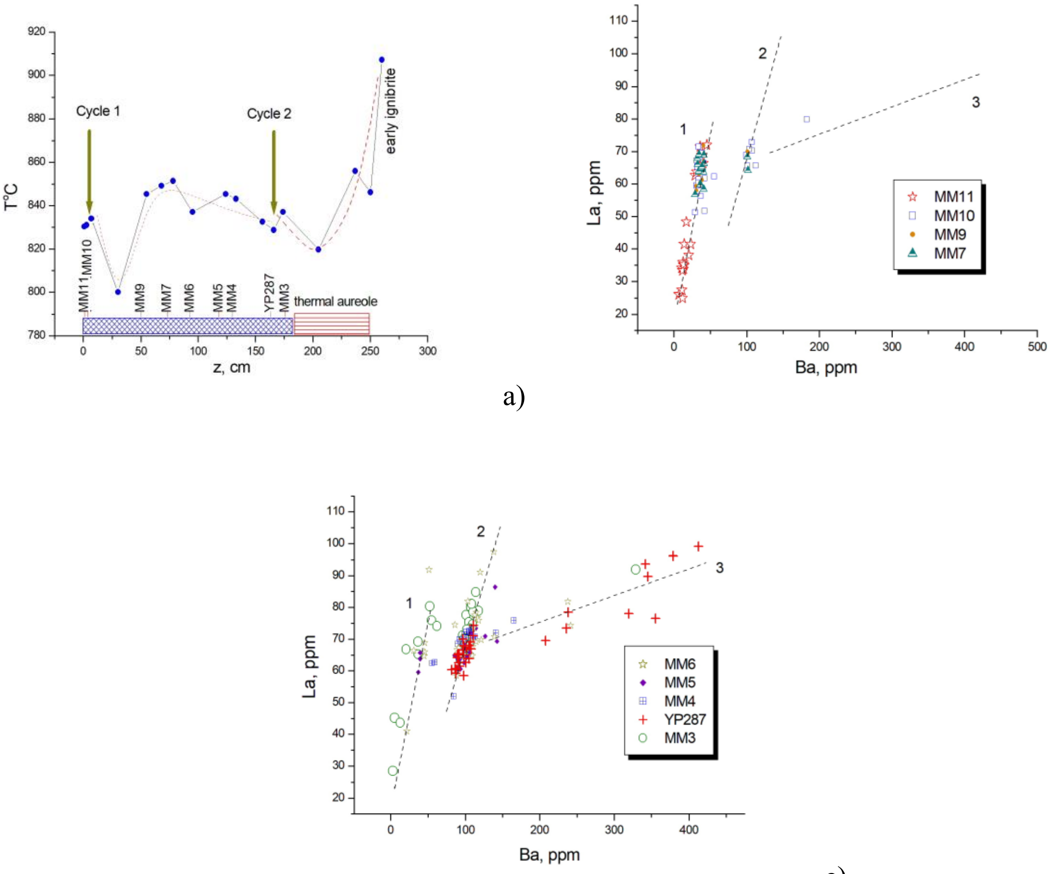

a)

b)

c)

Figure 10. Geochemical and mineralogical data for pre-HRT-A ash deposits a) upper temperature bounds from two-feldspar geothermometry [40]. The onsets of volcanic activity cycles are indicated. The thermal peak of the first cycle coincides with sample MM7. Devitrified glasses from the ignimbrite's thermal aureole were not analyzed by Myers [15]. b) compositions of volcanic glasses corresponding to the initial eruption phase (samples MM11–MM7; data from [15]). c) glass compositions from the subsequent eruption phase (samples MM6–MM3). The positions of three distinct compositional clusters are indicated by dashed lines.

4.1. Diffusional chronometry of water loss from MIs and embayments in quartz

Myers et al. [15] measured H_2O, CO_2 and trace element contents in glasses trapped as melt inclusions and embayments in quartz in ten horizons of a 2 m-thick ash layer. The authors concluded that the melts lost water during the hot phase of their history. The Rb cation has a large ionic radius and low diffusion mobility in the melt, reflecting the composition of the unaltered melt. Using the strong positive correlation between Rb and H_2O contents in the unaltered melt, the authors reconstructed the initial water content from the measured rubidium concentration in the glasses.

The statistical distributions of water loss (ΔC_w) as the difference between the estimated initial and observed water content in wt.% for the MIs and embayments have a similar left-skewed, close to log-normal shape (see Figure 11), with maximum values for both being 3.5 wt.%. Negative ΔC_w values for melt inclusions in Figure 11a arise because the estimated initial water contents are not exact and are subject to statistical error.

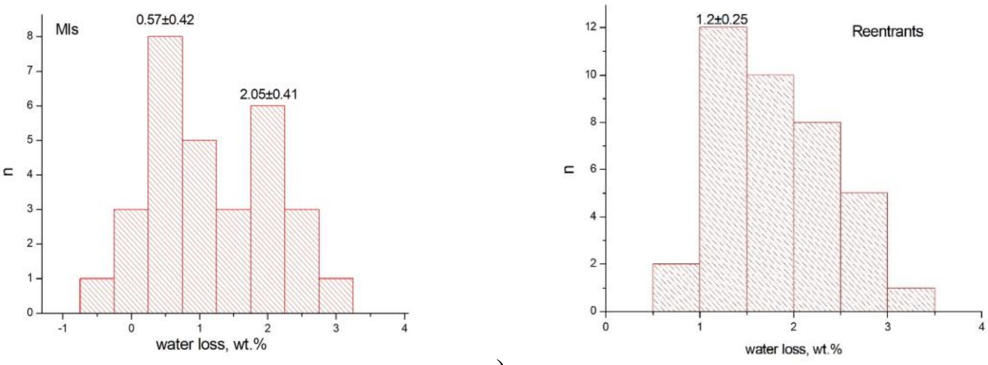

a) b)

Figure 11. Histograms of water loss by a) melt inclusions and b) reentrants in quartz from the pre-HRT-A phase of the Yellowstone eruption, estimated from supplementary data to [15].

The minimum values of ΔC_w for the MIs are 0.57 ± 0.42 wt.%, and for the reentrants −1.2 ± 0.25 wt.% (see Figure 11). The initial water content in the melt is about 4.5 wt.%, the minimum water content in the reentrants is 1.2–1.5 wt.%. Using the results of numerical experiments (see Figure 8), the diffusion time of the reentrants was estimated at 1.2 ÷ 2.9 hours. The following parameter values were used: maximum L = 200 μm, T = 750–850°C, $C_{H2O,0} = 4.0$ wt.%, $\Delta C = 1.2$–1.5 wt.%, we employ the *Cb(t)* expressions for Mode 1 and Mode 2. These estimates of diffusion time translates to decompression rate of ~0.02–0.06 MPa/s.

Similarly, the minimum diffusion water loss for MIs can be estimated using Equation (10). We use the following parameter values: inclusion radius of 31 μm (corresponds to the average value obtained in Figure 2 in [15]), water diffusion coefficient in quartz $lg(D_w) = -11.2$ m^2/s, $k_r = 1.5e{-}04$. At $\Delta C = 0.57$ wt.%, the diffusion time is 19.6 hours. The diffusion coefficient of water in quartz depends on the defect concentration and can vary significantly. The distribution coefficient k_D, proportional to the maximum water content in quartz, is also not constant, so these estimates can be considered approximate. At $k_D = 4.5e{-}04$, the diffusion time estimate decreases to 6.5 hours. The experimental data [14] show that rapid water loss via H_2 diffusion/Fe oxidation yields a dehydration timescale of ≤4 hours for MIs. Applying this mechanism to the pre-HRT-A eruption provides a minimum natural diffusion time for MIs. This minimum estimate is consistent with the maximum diffusion time of ~3 hours obtained for reentrants from Figure 11b. The agreement between these bounding values indicates that both MIs and reentrants dehydrated during the same brief event, interpreted as syneruptive degassing.

Larger values of water loss for MI are formed not due to diffusion but due to leakage caused by plastic failure of quartz, probably due to the melt vesiculation or by the mechanicall stresses caused by eruption [46].

4.2. Correlation of Li, CO_2, and H_2O contents in melt inclusions

Meyers et al. [15] provided extensive information on the composition of melt inclusions and reentrants in quartz, enabling analysis of fluid-magma interactions during eruption initiation and progression. Volatiles (CO_2, H_2O) and lithium are rapidly diffusing species [29], with rates comparable to those of intrachamber and syneruptive degassing. Lithium is typically lost with water during vesiculation. However, it has been shown that lithium can also be transported into magma via CO_2-enriched fluid [47].

Table 1. Representation of concentration of Li in MIs as linear function of C_{H2O} and C_{CO2}.

layer	C_{CO2}, ppm	C_{H2O}, wt.%	a^{*} [##]	b	$R_{calc,obs}$.	1σ	comments
MM3[#]	203 (149)###	2.88 (1.14)	−14.59	11.7	0.76	19.63	prolonged interaction with CO_2 enriched melt or fluid
YP287	180 (101)	2.48(0.96)	−9.36	12.6	0.95	6.19	
MM4	503 (158)	3.02 (0.93)	−8.05	12.8	0.75	10.8	syn-eruptive water loss and MIs leakage
MM5	467 (220)	2.83 (0.89)	−31.27	21.5	0.76	8.05	
MM6	225 (34)	2.82 (0.71)	0.04	15.7	0.79	11.3	
MM7	120 (42)	3.06 (1.19)	−0.96	16.0	0.99	2.32	
MM9	417 (87)	2.62 (0.98)	−1.12	20.1	0.95	6.15	
MM10	223 (130)	3.14 (0.77)	−15.18	26.4	0.77	12.92	
MM11	279 (110)	3.35 (1.04)	29.01	6.3	0.91	7.16	flushing by Li enriched CO_2 fluid

Note: [#] lines with poor fit of Li variations are shaded in grey; [##] regression coefficient a is multiplied on the average CO_2 concentration; [##] average (standard deviation).

We analyzed the covariance of Li concentrations with H_2O and CO_2 in MIs by means of linear regression analysis. The Li dataset was approximated using a least-squares fit as a linear function of CO_2 and H_2O concentrations. The results are presented in Table 1:

$$C_{Li} = aC_{CO2} + bC_{H2O} + d, \tag{13}$$

The value of coefficient a (in ppm^{-1}) in Table (1) is presented in the dimensionless form $a^* = a\widehat{C_{CO2}}$, where $\widehat{C_{CO2}}$ is the average CO_2 concentration for given sample. This scaling brings its magnitude closer to that of coefficient b (in $wt.\%^{-1}$) for easier comparison.

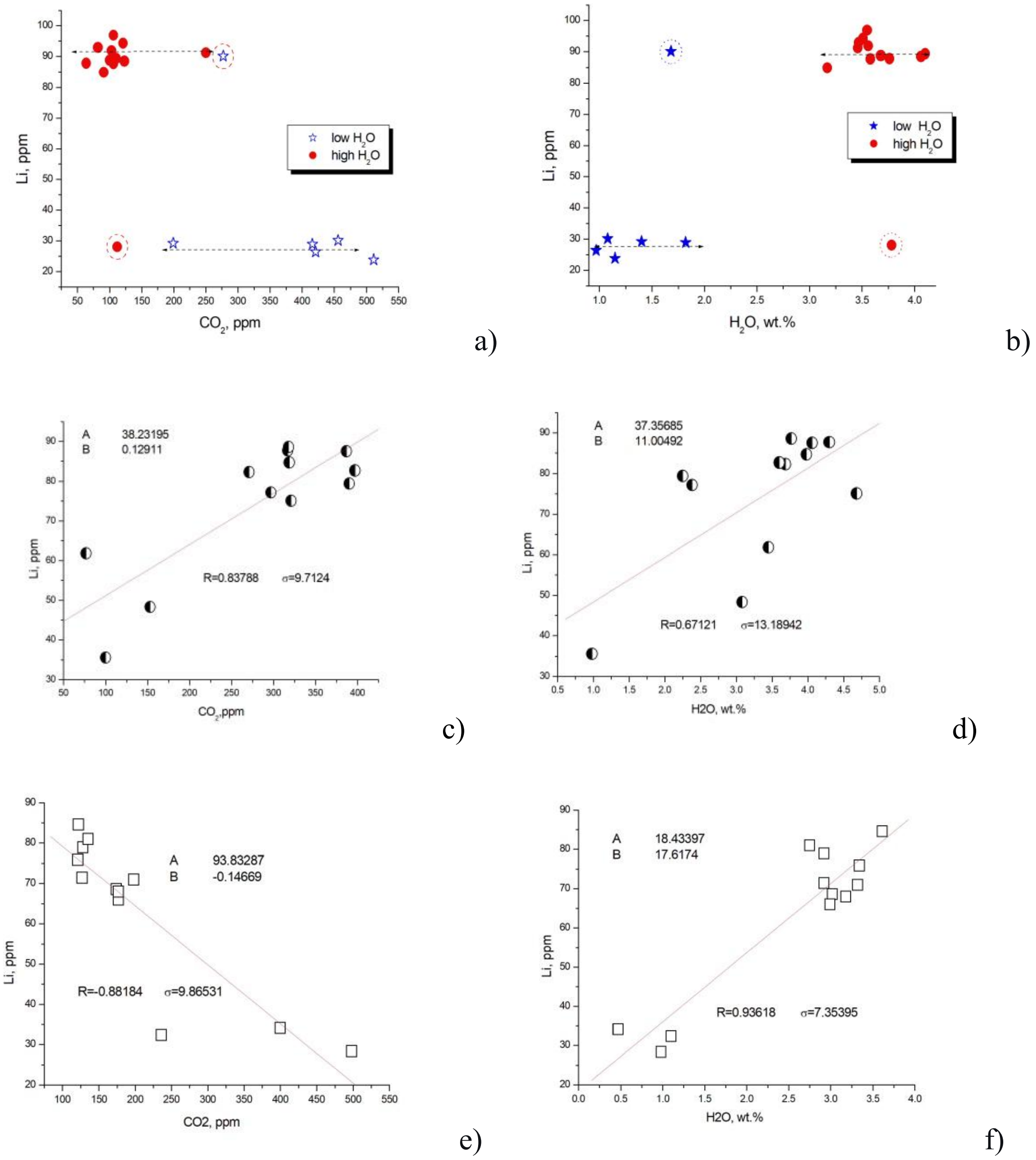

a) b)

c) d)

e) f)

Figure 12. Relationships between Li and volatile components (H_2O, CO_2) in melt inclusions. Plots illustrate contrasting pair correlations across three samples: a,b) MM3 (uncorrelated), c,d) MM11 (positive Li–CO_2 correlation), and e,f) YP287 (negative Li–CO_2 correlation). Data from [15] supplementary material.

Linear approximation effectively reproduces the variation in Li concentration for compositionally homogeneous samples, which form a compact cluster of data points in Figure 10 *b,c*. Samples YP287, MM7, MM9, and MM11 show a high correlation coefficient ($R > 0.9$) between the observed Li concentrations and those calculated from Equation (13). In contrast, variations in Li content for samples with $R < 0.8$ cannot be explained solely by changes in CO_2 and H_2O contents (see Supplementary File S1).

Sample MM3 exhibits the weakest bilinear approximation among the studied samples, with a correlation coefficient of R = 0.76 and a standard deviation of $\sigma = 19.6$ between calculated and measured Li values (see Supplementary File S1). The scatter in the data can be explained by the presence of two distinct compositional groups visible on the pairwise correlation plots: a high-water group and a uniform low-water group (Figure 12a,b). Within each group, Li concentrations are practically uniform, showing no significant dependence on either CO_2 or H_2O, with the exception of a single outlier point in each.

The best correlation ($R = 0.99$) and smallest standard deviation ($1\sigma = 2.32$ ppm) were obtained for sample MM7. The largest standard deviation ($1\sigma = 19.63$ ppm) was shown by sample MM3, whose composition falls within all three clusters on the diagram in Figure 10b,c.

As expected for lithium transport to a fluid phase during vesiculation and water loss from melt inclusions, a positive covariance between Li and H_2O is observed for all samples. Notably, CO_2 appears to have negligible influence on Li behavior in samples MM9 and MM7. Conversely, the weakest relationship between Li and H_2O and a strong positive correlation between Li and CO_2 was found in sample MM11. The bilinear approximation (Eqn.13) of Li concentration offers a significant advantage over simple pairwise correlations. This is demonstrated for sample MM11 (see Figure 12c,d). The pairwise correlations of Li with CO_2 (R = 0.84, $\sigma = 9.7$) and with H_2O (R = 0.67, $\sigma = 13.2$) are notably weaker than the fit achieved by the bilinear model (R = 0.91, $\sigma = 7.2$; see Supplementary File S1). The strength of this bilinear correlation suggests that CO_2 and Li were introduced into the melt simultaneously.

A significant negative covariance between Li and CO_2 was identified for sample YP287. For this sample effect of prevalence of bilinear approximation is weaker. Powers of the paired correlations are close: for Li-CO_2 correlation coefficient R= −0.88 and $\sigma = 9.9$, and for Li-H_2O, R = 0.94 and $\sigma = 7.4$ (Figure 12e,f). Water-lithium paired correlation is almost as strong as $Li_{calc}(Li_{meas})$ for bilinear representation R = 0.95 $\sigma = 6.2$. Therefore, Li behavior can be interpreted as coupled H_2O and Li loss at CO_2 induced dehydration. The nature of these correlaitons will be discussed in the next section. The distribution of average CO_2 concentration in melt inclusions with depth is uneven (Table 1). The minimum CO_2 content occurs in sample MM7, from the center of the ash column, and is four times lower than the concentrations in the layers above (MM4) and below (MM9).

4.3. Interpretation of the contrast covariance of Li with CO_2

4.3.1. How can the position of the sample in the ash sequence be related to the position of the corresponding piece of magma in a chamber?

Each sample within an ash layer can incorporate material from multiple depths within a single magma body or from several distinct, spatially separated bodies. Furthermore, ash sedimentation with grain-size sorting (e.g., [48]) can locally influence the composition at specific points in the ash sequence. In this study, we neglect the potential effects of sedimentation and size sorting, assuming that the entire ash layer originates from a single magma layer.

A conceptual framework for understanding erupted ash composition is provided by the simplified magma withdrawal model of Spera [49]. This model demonstrates that material points located along evacuation isochrones simultaneously reach the entrance to the volcanic conduit at a given moment, thereby contributing to a specific eruptive parcel. The model predicts that, under conditions of constant eruption intensity, the evacuation zone deepens and expands laterally over time. Following the withdrawal and flushing of the single-volume models, we can expect the eruption sequence to evolve. Initially, the ash will be dominated by the first near bottom magma portion ascending and triggering eruption (zone 1 in Figure 5). Over time, the erupted material will become increasingly dominated by later, near-roof magma from zones 4 and 3. At some point, this may be followed by the entrainment of deeper, less-evolved magma from zone 2. Finally, as the eruption rate declines, the zone of magma withdrawal will contract back toward the roof, with the final phase sourced predominantly from zone 3.

4.3.2. MIs and reentrants compositions on H_2O-CO_2 diagram—correlation with magma dynamics in a chamber during eruption

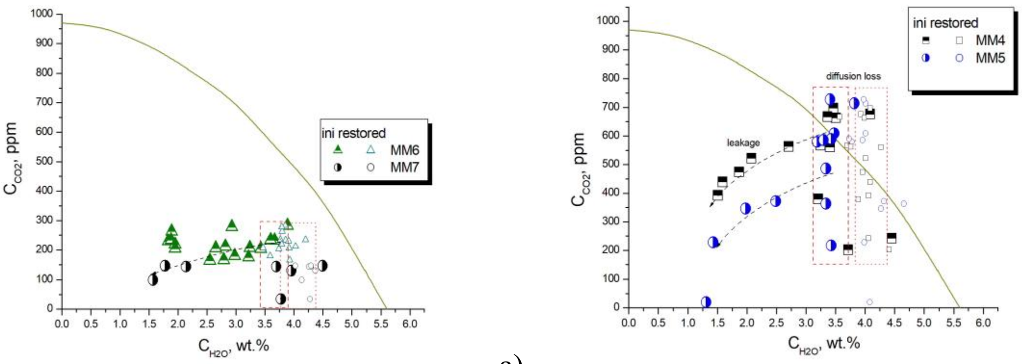

a) b)

Figure 13. Volatile contents in melt inclusions data (from the supplementary material to [15]) for samples a) MM6 and MM7 presumably represent the deepest erupted magma b) melt inclusions from samples MM4 and MM5 probing near roof magma. In both groups two populations of syn-eruptively dehydrated and leaked melt inclusions can be distinguished; trends toward a significant decrease in H_2O content combined with a slight decrease in CO_2 content in the leaked melt inclusions are shown by arrows. Dashed rectangles indicate the initial and syneruptively modified water content in the unleaked melt inclusions. Semi-filled symbols correspond to the original measurements, while open symbols correspond to the estimated initial composition. Solubilily of CO_2-H_2O fluid in the rhyolitic melt at P = 200 MPa (continuous line) is from [50].

The arguments considered above allow for a petrologically-based interpretation of CO_2–H_2O diagrams for melt inclusions and reentrants at different stratigraphic positions. For the presumably deepest sample MM7 and similar MM6, the MIs (Figure 13a) and reentrants (Figure S1.1, Supplementary file S1) have virtually identical restored compositions: low CO_2 contents (100–200 ppm) and approximately 4–4.5 wt% H_2O, which lie far below the saturation curve.

In accordance with our interpretation, samples MM10, MM9, MM5, and MM4 represent near-roof magma. Sample MM9, which records the minimum two-feldspar temperature (see Figure 10a), is positioned closest to the upper boundary layer. MI data from MM9 with the highest H_2O and CO_2 contents (both measured and restored) plot near the fluid saturation curve at 200 MPa (see Figure S1.2, Supplementary file S1). Sample MM10 is similar but exhibits a slight offset above the saturation curve for several inclusions.

Some MIs from samples MM4 and MM5 (both measured and restored) show a significant offset above the saturation curve (see Figure 13b), for which equilibration pressures are estimated at 260–280 MPa. In contrast, the restored compositions for MM10 reentrants (Figure S1.3) are well characterized and fall directly on the solubility curve at 200 MPa, consistent with the final near-roof position of the probed magma. The maximum pressure estimates likely correspond to melt inclusions reaching fluid saturation during CO_2 fluxing at near-bottom depths. This pressure range implies a magma chamber height of approximately 1.7 km. Another possible explanation involves the rehydration of melt inclusions formed from dehydrated magma. Diffusive transport of H_2O (not CO_2) through the host quartz crystal can equilibrate the water content between the inclusion and the more hydrous external magma. This process may potentially shift the data points above the saturation curve. Additional information, such as isotope data, is required to estimate the relative contributions of both potential mechanisms to the observed apparent high pressures of melt inclusion entrapment.

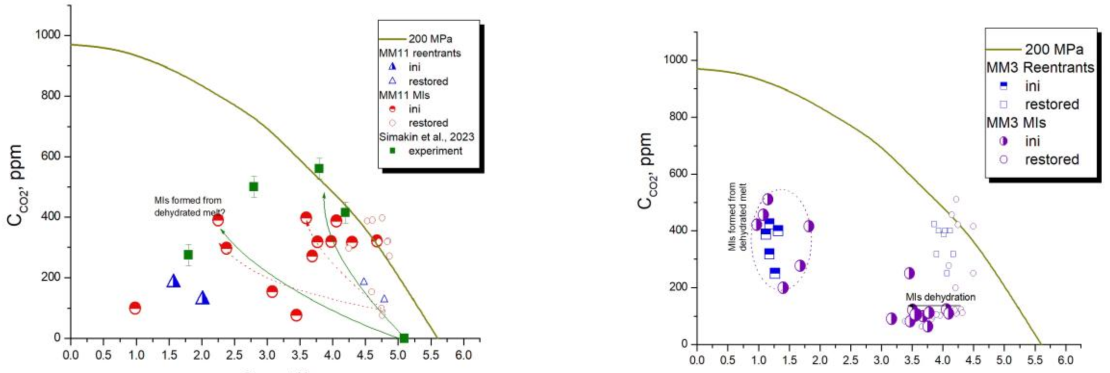

a) b)

Figure 14. Volatile contents in glass data (from the supplementary material to [15]) for samples related to the initiation of HRT-A eruption cycles. a) Sample MM11, characterized by high initial H_2O and the most fractionated composition (see Figure 10b). For comparison, compositions from experimental CO_2-flushing of hydrous albite melt [9] are plotted b) Sample MM3, only low-H_2O reentrants were identified, revealing two distinct groups of melt inclusions: one with low CO_2 and minimal H_2O loss, and another with low H_2O and variable CO_2 concentrations. See text for interpretation.

Sample MM11 (see Figure 14a) represents the composition of the portion of magma that presumably emerged from the lower zone and triggered the first eruption cycle. The composition of the melt inclusions can be interpreted as reflecting varying degrees of dehydration and CO_2 enrichment during flushing of the lower layer with juvenile lithium-rich CO_2 (resulting in a positive correlation between Li and CO_2). The growth rate of quartz is low, so these inclusions must have formed well before the convective overturning in a sequence of minor CO_2 flushing events preceding the critical one. Sample YP287 (Figure S4) showed a similar pattern. This flushing event presumably initiated the second eruption cycle. However, the correlation between Li and CO_2 is negative, implying a fluid with a composition different from that of the fluid that initiated the first cycle. In our experiments [9], a similar chaotic compositional pattern was demonstrated for a hydrated albite melt dehydrated by passing CO_2 bubbles. The starting material was glass powder with an initial porosity of approximately 40 vol.%, filled with CO_2. At high temperatures, bubbles of various sizes formed, merged, and floated to the surface. Within a short time (40 min), the volume fraction of bubbles decreased to approximately 9 vol.%. The melt dehydrated and became saturated with CO_2 to varying degrees, forming compositions far from the uniformly dehydrated sequences shown in Figures 1 and 4.

It should also be noted that two populations of melt inclusions (preserved and leaked) are present in all samples except MM3, MM11, and YP287. In the preserved group, MIs show similar observed and restored compositions, indicating only minor syn-eruptive diffusive H_2O loss (~0.3 wt.%). Both their observed and restored compositions fall below the saturation curve at 200 MPa. The second dataset follows degassing trajectories indicative of rapid, non-equilibrium H_2O loss accompanied by a slower decrease in CO_2 content due to post-entrapment leakage (for samples MM4–MM5, see Figure 13b; for MM9–MM10, see Figures S2 in Supplementary File S1).

The composition of sample MM3 is extremely diverse and falls into all three clusters in the Figure 14b diagram, which is reflected in the inaccuracy of the multicorrelation for Li (see Supplementary File S2). Two groups are distinguished in the H_2O-CO_2 composition diagram. In the first group, the CO_2 content is only 100 ppm and the reduced and observed water contents are similar and vary in the range of 3–4 wt%. In the second group, the inclusions have a low water content of 1–1.5 wt% and a variable CO_2 content of 200–500 ppm, which coincides with the composition of the reentrants. The possible origin of the unusual inclusions and reentrants of sample MM3 will be discussed below.

5. Discussion

Recent application of a novel analytical method (synchrotron-based FTIR spectroscopy) has provided evidence for active CO_2 flushing during the Mesa Falls Tuff eruption of the Yellowstone supervolcano [37]. The authors performed precise analyses of reentrants (embayments) in quartz along profiles with a measurement spot size of 3 μm (compared to 20 μm spots in [33]). The H_2O distribution within these embayments appears nearly uniform, except for a sharp concentration increase in the open neck region attributed to secondary low-temperature hydration. In contrast, CO_2 profiles exhibit a steep concentration gradient, decreasing toward the contact with the surrounding volcanic glass of the groundmass. The authors interpret the low and uniform H_2O concentration (~1 wt.%) in the embayments as a result of flushing by CO_2-rich fluids. These analyzed inclusions are compositionally quite similar to the melt inclusions and reentrants observed in the sample MM3 considered above.

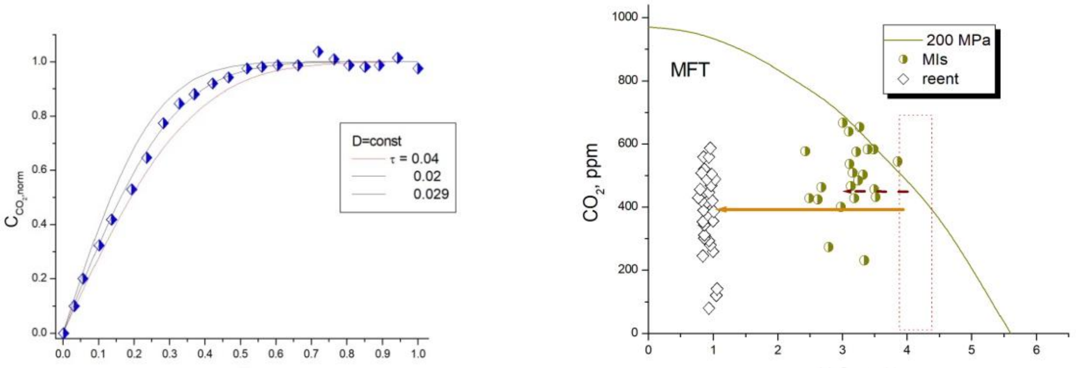

a) b)

Figure 15. Analytical data on the composition of melt inclusions and embayments from the MFT eruption, Yellowstone (from [37]) a) The CO_2 distribution in the embayment is perfectly approximated by the erfc function with a dimensionless time of 0.029. b) The dashed rectangle marks the boundaries of the inferred initial melt composition. Reentrants lost about 3–3.5 wt% (indicated by arrow) of water, while MIs could lose about 1 wt% (indicated by dashed arrow) if all the water was exsolved by the fluxing with CO_2 fluid.

The CO_2 distribution reported by Befus et al. [37] exhibits a plateau shape (Figure 15a), indicating limited penetration of the diffusion front and retention of the initial concentration near the closed end of the embayment. The complementary error function (*erfc*) solution, assuming a constant diffusion coefficient, provides an excellent fit to the analytical data (minimum standard deviation = 0.009) for a dimensionless diffusion time of $\tau = 0.029$. If the observed water content of ~1 wt.% resulted from CO_2 flushing and decompression involved only CO_2 release while H_2O was mostly retained, then $\tau = 0.029$ corresponds to a physical diffusion time of 6.8 hours (assuming $C_{H2O,0} = 1$ wt%, T = 800°C) or 4.6 hours with minor concurrent water degassing ($C_{H2O,0} = 1.5$ wt%).

The diffusion time required to reduce the water content to 1 wt.% is considerably longer. The initial water content in the embayments can be estimated at approximately 4–4.5 wt.%, corresponding to the composition with maximum CO_2 content on the saturation curve at P = 200 MPa (see Figure 15b). During eruption, this was reduced to 1 ± 0.2 wt.%. If water was exsolved via flushing by a CO_2-enriched fluid, the boundary concentration (*Cb*) decreased gradually. For a first-order estimate of the diffusion time, we employ the *Cb(t)* expressions for Mode 1 and Mode 2. Using the dependences for $C_{H2O,max}$ in Figure 8, we obtain dimensionless diffusion times (τ) of 22.5 and 70 for Modes 1 and 2, respectively (neglecting the time required for $C_{H2O,max}$ to decrease from 5 to 4.5 wt.%). Given an embayment length L = 330 μm, T = 800 °C, and P = 200 MPa, the corresponding physical diffusion times are 18.7 and 58.2 hours for $C_{H2O,0} = 5$ wt.% and 24.8 and 77.2 hours for $C_{H2O,0} = 4.5$ wt.%. These values represent minimum estimates and actual times could be longer.

Under the same boundary conditions, melt inclusions could lose 1–1.5 wt.% H_2O (see Figure 15b) over several days of exposure. Using Equation (10) with a H_2O diffusion coefficient of 6.3 × 10^{-8} cm^2/s and a minimum melt inclusion radius of 70 μm [37], we obtain diffusion times of 46.5 and 77.3 hours for ΔC_{H2O} = 1 wt.% and 1.5 wt.%, respectively. As discussed above, the diffusion coefficient of H_2O in quartz is not a unique function of temperature and depends on defect concentration. Furthermore, the distribution coefficient k_D in Equation (10) is also variable. Therefore, the accuracy of this estimate is limited. Taken together, data from both melt inclusions and embayments constrain the minimum timescale for significant H_2O diffusion to be on the order of several days.

Assuming the uniform high-CO_2 and low-H_2O signature of reentrants results from CO_2 fluxing, the diffusion time needed to increase CO_2 from ~200 ppm to a uniform ~600 ppm (Figure 15b) can be constrained. Using Equation 12, and defining uniformity as within a 20 ppm uncertainty (normalized concentration of 0.95), the required non-dimensional time is $\tau = 1.31$. For a 330 μm reentrant, this translates to 4–8 days at 1.5 wt.% H_2O and temperatures of 850°C and 800 °C, respectively. These estimates are broadly consistent with the 2–3-day dehydration timescale for MIs.

CO_2 diffusion time is related to the final magma ascent, corresponding decompression rate was 0.008–0.012 MPa/s (ascent rate 0.3–0.4 m/s). If correct, this estimate is close to the lower boundary of the interval of rates reported for HRT Yellowstone 0.013–0.059 MPa/s (0.007–0.118 within 2σ interval) [37].

However, the CO_2 fluxing hypothesis here faces two significant challenges. First, achieving such a profound reduction in H_2O content would require an implausibly large volume of carbonic fluid, approximately 80–100% of the magma volume. It is highly unlikely that this mechanism could dehydrate substantial magma bodies to the observed degree. Second, nearly dry silicic melts have high liquidus temperatures (up to 950–1100 °C). If a magma initially containing ~4 wt.% H_2O (with a liquidus temperature of 800–850 °C) were dehydrated, it would rapidly crystallize. In our experiments, an albite melt (a model composition for rhyolitic magma) crystallized by 80% within 4–5 hours when its H_2O concentration dropped from 5.1 to 2.5 wt.% due to interaction with a CO_2-rich fluid.

An alternative mechanism to generate H_2O-poor reentrants and melt inclusions involves mixing quartz crystals from the basal crystal mush with a hot, low-water melt produced by partial melting of the mush or cumulate at its contact with underplated basalts. Subsequently, over the timescales estimated above, this assemblage would undergo dehydration. Quartz crystals would remain stable if the melt is in equilibrium with granite cotectic minerals. This mechanism may be relevant to the formation of the glass compositions observed in sample MM3. The low-CO_2 melt inclusions could represent the melt composition in contact with mush crystals, where dehydration of 1–1.5 wt.% H_2O could occur, analogous to the process inferred for the MFT melt inclusions. The group of low-H_2O, variable-CO_2 melt inclusions may form during the interaction of the mush with this hot, dry melt.

The minimum timescales (2–3 days for dehydration of MFT melt inclusions and 4–8 days for CO_2 saturation of reentrants) constrain how long a CO_2-rich fluid and/or a dehydrated magma can interact with the loose crystal mush in the near-bottom boundary layer prior to the development of convective instability. Meanwhile, the minimum diffusion times of water (pre-HRT-A) and CO_2 (MFT) estimated for quartz reentrants from Yellowstone eruptions indicate an upper limit for magma ascent rates during eruption of 0.3–2.1 m/s.

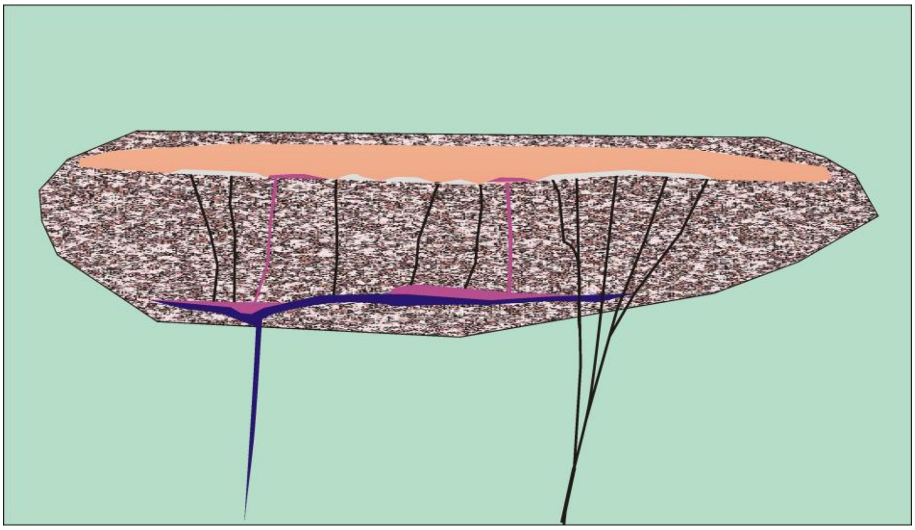

Figure 16. Cartoon of the proposed mechanism for initiating the pre-HRT-A ashfall eruption. The massive intrusion of basaltic magma (blue) induced melting of cumulates with low residual melt content (speckled brown), generating hot, dry rhyolitic melt (dark red). CO_2 (fractured pathways indicated by black) and, subsequently, the hot, dry rhyolitic melt migrated through the partial melt zone to the base of the overlying magma lens. CO_2 fluxing produced a buoyant, bubble-rich boundary layer at the base of the lens. The ascent of this layer to the roof initiated the first explosive eruption of evolved rhyolites. In the second stage, the ascent of buoyant plumes of both the pre-existing and newly formed bubbly magmas triggered the eruption of ignimbrites. See text for further details.

The proposed scenario for triggering the pre-HRT-A ashfall is schematically depicted in Figure 16. It illustrates how, within a large volume of partial melt (melt fraction 10–15 vol.%) at a depth of approximately 7 km (as inferred for quiescent periods from geophysical data, e.g., [51]), a lens of crystal-poor magma accumulates prior to the eruption.

Continued underplating by basaltic magma generates new batches of hot, dry melt (depicted in dark red in Figure 16). This melt, along with CO_2, migrates through fractures in the partial melt zone and reaches the base of the evolved magma lens. The grey layers at the base represent bubble-rich magma. The ascent of this buoyant, bubbly material can cause a rapid increase in advective overpressure [6]. Since fluid density is strongly pressure-dependent, the rise of bubbles in a relatively incompressible medium (liquid magma within a confined reservoir) can transfer hydrostatic pressure upward. That is, to maintain a constant volume, a rising bubble necessitates an increase in pressure at the reference depth (e.g., the chamber top) by an amount equivalent to the hydrostatic pressure of the magma column. In reality, due to the finite compressibility of magma and the flexibility of the chamber roof, this effect is reduced by a factor of several.

As considered earlier, the actual height of the magma lens is uncertain. If the highest pressure estimates from melt inclusions are not entirely result of post-entrapment rehydration, the lens height could be on the order of 1.7 km. This could generate an overpressure of approximately ≈ (60–70)/3 MPa, or 20–25 MPa, which may be sufficient to initiate an eruption. Pressure would also increase due to the intrusion of basalts into the mush zone, causing additional melting. However, mechanical stresses induced by magma input are partly mitigated by viscous relaxation within the thermal aureole of the magma body [52,53]. Consequently, magma overpressure and the resultant stress in the host rock are proportional to the ratio of the magma input rate to the chamber volume. Therefore, a critical magma input rate is required to achieve stress levels sufficient for dyke propagation (which would establish a volcanic conduit) or for roof failure.

In the proposed model, the rapid transport of deep, hot, juvenile CO_2 through the lower parts of the magmatic system could induce rapid dehydration and convective overturn of a bubble-rich layer near the chamber base over timescales of hours to days. Models that neglect such intra-chamber vertical movements of vesiculated magma and the effects of CO_2-induced dehydration conclude that volatiles have no significant impact on the effective magma volumetric input rate [54]. In contrast, we argue that the rapid pressure buildup during fluid-magma interaction, potentially faster than that caused by basalt intrusion or melting, may inflict significant mechanical damage to the chamber roof, potentially leading to its fragmentation along pre-existing regional faults.

The relative importance of CO_2 fluxing versus silicic mush rejuvenation by basalt underplating in triggering eruptions is still unresolved and scales with the mass of injected CO_2. Our evidence for early CO_2-fluid arrival at the base of the magma layer on the top magma chamber could thus mark either the precursor to a hot rhyolite invasion or the actual trigger of Yellowstone eruptions.

6. Conclusions

1. Modeling of the flushing of rhyolite magma by carbon dioxide-enriched fluid at the micro level of an individual bubble in the spherical shell approximation showed uniform melt dehydration at the first stage. The numerical model takes into account the effect of the dependence of the diffusion mobility of water and CO_2 on the water concentration. With a realistic content of free fluid and bubble size, dehydration preceding CO_2 saturation takes from fractions of an hour to several hours.
2. The effect of intra-chamber degassing can be recorded in the composition and compositional gradient of melt inclusions and embayments in quartz, along with the effect of decompression-induced volatile release. Decompression can also induce an initial dehydration regime that differs from equilibrium degassing in open and closed systems, which begins with CO_2 release. Given such a variety of regimes, it makes sense to roughly estimate the independent diffusion times of CO_2 and H_2O using exponential decay in time relationships between the maximum (for reentrants) and average (for MI) concentrations at long dimensionless times ($\tau > 2–4$). We numerically calculate such time-dependences for reentrants in 1-D under several degassing regimes.
3. The susceptibility of MIs to synerruptive and intrachamber water loss (and gain) was quantified by analyzing published experimental data. We found that the high-temperature water diffusion coefficient in quartz, calculated from published experimental data on the loss of H_2O from MIs in quartz over time, is in good agreement with values obtained using standard diffusion measurement methods. MIs rehydration and deep dehydration to water contents of approximately 1 wt% imply long diffusion times of days or more.

4. An analysis of published data on the eruption immediately preceding phase A of the Yellowstone HRT eruption was conducted. A regression analysis of lithium contents in melt inclusions as a function of CO_2 and H_2O revealed a generally significant positive regression and correlation coefficients between lithium and water and an insignificant ones with CO_2, which is explained by the removal of lithium and water into the fluid phase during degassing. A significant correlation between lithium and CO_2 was found at two levels. The correlation coefficient is positive at the bottom of the ash column and negative at the top. It is assumed that the eruption can begin after the ascent of a bottom layer of magma that reacted with juvenile (basaltic or mantle) lithium-enriched CO_2.

Author contributions

Alexander Simakin: conceptualization (lead); methodology (lead), software (lead); validation (equal); writing–original draft (lead); formal analysis (lead); writing–review and editing (equal); visualization (equal). Vera Devyatova: validation (equal); writing–review and editing (equal); visualization (equal).

Use of AI tools declaration

The authors declare they have not used Artificial Intelligence (AI) tools in the creation of this article.

Acknowledgments

For AS and VD, this study was supported by ongoing institutional funding, theme FMUF-2022-0004 of the Institute of Experimental Mineralogy, Russian Academy of Sciences. The authors thank ananimous reviewers for their helpful reviews, which prompted a substantial revision of the geological application and improved the presentation of the numerical modeling results and the theoretical estimate of the water diffusion coefficient in quartz. Andrey Shiryaev provided significant assistance in obtaining analytical data from the experimental samples, which were crucial for interpreting the petrological data.

Conflict of interest

All authors declare no conflicts of interest in this paper

References

1. Huppert H, Woods AW (2002) The role of volatiles in magma chamber dynamics. *Nature* 420: 493–495. https://doi.org/10.1038/nature01211

2. Simakin AG, Ghassemi A (2018) Mechanics of magma chamber with implication to the effect of CO_2 fluxing, *Volcanoes: Geological and Geophysical Setting, Theoretical Aspects and Numerical Modeling, Applications to Industry and Their Impact on the Human Health*, 175–207. http://dx.doi.org/10.5772/intechopen.71655
3. Thomas N, Tait S, Koyaguchi T (1993) Mixing of stratified liquids by the motion of gas bubbles: application to magma mixing. *Earth Planet Sci Lett* 115: 161–175. https://doi.org/10.1016/0012-821X(93)90220-4
4. Simakin A, Schmeling H, Trubitsyn V (1997) Convection in melts due to sedimentary crystal flux from above. *Phys Earth Planet Inter* 102: 185–200. https://doi.org/10.1016/S0031-9201(97)00010-1
5. Steinberg GS, Steinberg AG, Merzhanov AG (1989) Fluid mechanism of pressure growth in volcanic (magmatic) systems. *Mod Geol* 13: 257–265.
6. Seropian G, Kennedy BM, Walter TR, et al. (2021) A review framework of how earthquakes trigger volcanic eruptions. *Nat Commun* 12: 1004. https://doi.org/10.1038/s41467-021-21166-8
7. Bagdassarov N (1994) Pressure and volume changes in magmatic systems due to the vertical displacement of compressible materials. *J Volcanol Geotherm Res* 63: 95–100. https://doi.org/10.1016/0377-0273(94)90020-5
8. Simakin AG (2010) The role of intercameral degassing of andesite magma of the Shiveluch volcano (Kamchatka). *Dokl Earth Sci* 431: 458–461. https://doi.org/10.1134/S1028334X10040100
9. Simakin AG, Devyatova VN, Shiryaev AA (2023) Theoretical and Experimental Modeling of Local Scale CO_2 Flushing of Hydrous Rhyolitic Magma. *Russ J Earth Sci* 23. https://doi.org/10.2205/2023es000871
10. Befus KS, Manga M (2019) Supereruption quartz crystals and the hollow reentrants Supereruption quartz crystals and the hollow reentrants. *Geology* 47: 710–714. https://doi.org/10.1130/G46275.1
11. Yoshimura S, Nakamura M (2010) Chemically driven growth and resorption of bubbles in a multivolatile magmatic system. *Chem Geol* 276: 18–28. https://doi.org/10.1016/j.chemgeo.2010.05.010
12. Yoshimura S, Nakamura M (2011) Carbon dioxide transport in crustal magmatic systems. *Earth Planet Sci Lett* 307: 470–478. https://doi.org/10.1016/j.epsl.2011.05.039
13. Yoshimura S, Nakamura M (2013) Flux of volcanic CO_2 emission estimated from melt inclusions and fluid transport modelling. *Earth Planet Sci Lett* 361: 497–503. https://doi.org/10.1016/j.epsl.2012.11.020
14. Severs MJ, Azbej T, Thomas JB, et al. (2007) Experimental determination of H_2O loss from melt inclusions during laboratory heating: Evidence from Raman spectroscopy. *Chem Geol* 237: 358–371. https://doi.org/10.1016/j.chemgeo.2006.07.008
15. Myers ML, Wallace PJ, Wilson CJN, et al. (2016) Prolonged ascent and episodic venting of discrete magma batches at the onset of the Huckleberry Ridge supereruption, Yellowstone. *Earth Planet Sci Lett* 451: 285–297. https://doi.org/10.1016/j.epsl.2016.07.023

16. Zelenski M, Simakin A, Taran Yu, et al. (2021) Partitioning of elements between high-temperature, low-density aqueous fluid and silicate melt as derived from volcanic gas geochemistry. *Geochim Cosmochim Acta* 295: 112–134. https://doi.org/10.1016/j.gca.2020.12.011
17. Kerrick DM, Jacobs GK (1981) A Modified Redlich Kwong equation of state for H_2O, CO_2, and H_2O–CO_2 mixtures at elevated pressures and temperatures. *Am J Sci* 281: 735–767. https://doi.org/10.2475/ajs.281.6.735
18. Nowak M,·Behrens H (1997) An experimental investigation on diffusion of water in haplogranitic melts. *Contrib Mineral Petrol* 126: 365–376. https://doi.org/10.1007/s004100050256
19. Zhang Y, Ni H (2010) Diffusion of H, C, and O Components in Silicate Melts. *Rev Mineral Geochem* 72: 171–225. https://doi.org/10.2138/rmg.2010.72.5
20. Watson EB (1991) Diffusion of dissolved CO_2 and Cl in hydrous silicic to intermediate magmas. *Geochim Cosmochim Acta* 55: 1897–1902. https://doi.org/10.1016/0016-7037(91)90031-Y
21. Yoshimura S (2015) Diffusive fractionation of H_2O and CO_2 during magma degassing. *Chem Geol* 411: 172–181. https://doi.org/10.1016/j.chemgeo.2015.07.003
22. Pichavant M, Di Carlo I, Rotolo SG, et al. (2013) Generation of CO_2-rich melts during basalt magma ascent and degassing. *Contrib Mineral Petrol* 166: 545–561. https://doi.org/10.1007/s00410-013-0890-5
23. Befus KS, Gardner JE (2016) Magma storage and evolution of the most recent effusive and explosive eruptions from Yellowstone Caldera. *Contrib Mineral Petrol* 171: 30. https://doi.org/10.1007/s00410-016-1244-x
24. Barth A, Plank T (2021) The Ins and Outs of Water in Olivine-Hosted Melt Inclusions: Hygrometer vs. Speedometer. *Front Earth Sci* 9: 614004. https://doi.org/10.3389/feart.2021.614004
25. Simakin AG, Bindeman IN (2022) Convective Melting and Water Behavior around Magmatic-Hydrothermal Transition: Numerical Modeling with Application to Krafla Volcano, Iceland. *J Petrol* 63: egac074. https://doi.org/10.1093/petrology/egac074
26. Anderson AT, Davis AM, Lu F (2000) Evolution of Bishop Tuff rhyolitic magma based on melt and magnetite inclusions and zoned phenocrysts. *J Petrol* 41: 449–473. https://doi.org/10.1093/petrology/41.3.449
27. Hencz M, Biró T, Kovács IJ (2021) Uniform "water" content in quartz phenocrysts from silicic pyroclastic fallout deposits – implications on pre-eruptive conditions. *Eur J Mineral* 33: 571–589. https://doi.org/10.5194/ejm-33-571-2021
28. Kats A (1962) Hydrogen in alpha-quartz. *Philips Res Rep* 17: 133–195, 201–279. https://resolver.tudelft.nl/uuid:ab91c719-f00b-4362-ade3-8d44db910980
29. Jollands MC, Ellis B, Tollan PME, et al. (2020) An eruption chronometer based on experimentally determined H-Li and H-Na diffusion in quartz applied to the Bishop Tuff. *Earth Planet Sci Lett* 551: 116560. https://doi.org/10.1016/j.epsl.2020.116560

30. Bachheimer JP (1998) An investigation into hydrogen stability in synthetic, natural and air-swept synthetic quartz in air temperatures up to 1100°C. *J Phys Chem Solids* S9: 831–840. https://doi.org/10.1016/S0022-3697(96)00164-3
31. Abdisa LT (2021) One Dimensional Heat Equation and its Solution by the Methods of Separation of Variables, Fourier Series and Fourier Transform. *J Appl Comp Math* 10: 1–6.
32. Ferguson DJ, Gonnermann HM, Ruprecht P, et al. (2016) Magma decompression rates during explosive eruptions of Kilauea volcano, Hawaii, recorded by melt embayments. *Bull Volcanol* 78: 71. https://doi.org/10.1007/s00445-016-1064-x
33. Myers ML, Wallace PJ, Wilson CJN, et al. (2018) Ascent rates of rhyolitic magma at the onset of three caldera-forming eruptions. *Am Mineral* 103: 952–965.
34. Myers ML, Wallace PJ, Wilson CJN (2019) Inferring magma ascent timescales and reconstructing conduit processes in explosive rhyolitic eruptions using diffusive losses of hydrogen from melt inclusions. *J Volcanol Geotherm Res* 369: 95–112. https://doi.org/10.1016/j.jvolgeores.2018.11.009
35. Myers ML, Druitt TH, Schiavi F, et al. (2021) Evolution of magma decompression and discharge during a Plinian event (Late Bronze-Age eruption, Santorini) from multiple eruption-intensity proxies. *Bull Volcanol* 83: 18. https://doi.org/10.1007/s00445-021-01438-3
36. Mutch EJF, Newcombe ME, Rudge JF (2024) 3D diffusion of water in melt inclusion-bearing olivine phenocrysts. *Geochem Geophys Geosyst* 25: e2023GC011365. https://doi.org/10.1029/2023GC011365
37. Befus KS, Ruefer AC, Allison CM, et al. (2023) Quartz-hosted inclusions and embayments reveal storage, fluxing, and ascent of the Mesa Falls Tuff, Yellowstone. *Earth Planet Sci Lett* 601: 117909. https://doi.org/10.1016/j.epsl.2022.117909
38. Gordeychik B, Churikova T, Shea T, et al. (2020) Fo and Ni relations in olivine differentiate between crystallization and diffusion trends. *J Petrol* 61: egaa083. https://doi.org/10.1093/petrology/egaa083
39. Neukampf J, Laurent O, Tollan P, et al. (2022) Degassing from magma reservoir to eruption in silicic systems: The Li elemental and isotopic record from rhyolitic melt inclusions and host quartz in a Yellowstone rhyolite. *Geochim Cosmochim Acta* 326: 56–76. https://doi.org/10.1016/j.gca.2022.03.037
40. Swallow EJ, Wilson CJ, Myers ML, et al. (2018) Evacuation of multiple magma bodies and the onset of caldera collapse in a supereruption, captured in glass and mineral compositions. *Contrib Mineral Petrol* 173: 33. https://doi.org/10.1007/s00410-018-1459-0
41. Christiansen RL (2001) *The quaternary and pliocene Yellowstone Plateau volcanic field of Wyoming, Idaho, and Montana*, US Department of the Interior, US Geological Survey. 729.
42. Stelten ME, Cooper KM, Vazquez JA, et al. (2015) Mechanisms and timescales of generating eruptible rhyolitic magmas at Yellowstone caldera from zircon and sanidine geochronology and geochemistry. *J Petrol* 56: 1607–1642. https://doi.org/10.1093/petrology/egv047
43. Wilke S, Klahn C, Bolte T, et al. (2015) Experimental investigation of the effect of Ca, Fe and Ti on cotectic compositions of the rhyolitic system. *Eur J Mineral* 27: 147–159. https://doi.org/10.1127/ejm/2015/0027-2423

44. Zakirov IV, Sretenskaja NG, Aranovich LY, et al. (2007) Solubility of NaCl in CO_2 at high pressure and temperature: First experimental measurements. *Geochim Cosmochim Acta* 71: 4251–4255. https://doi.org/10.1016/j.gca.2007.01.028
45. Berkesi M, Guzmics T, Szabo C, et al. (2012) The role of CO_2 rich fluids in trace element transport and metasomatism in the lithospheric mantle beneath the Central Pannonian Basin, Hungary, based on fluid inclusions in mantle xenoliths. *Earth Planet Sci Lett* 331–332: 8–20. https://doi.org/10.1016/j.epsl.2012.03.012
46. Befus KS, Manga M, Stan C, et al. (2019) Supervolcanoes erupt stressed quartz crystals. *Geophys Res Lett* 46: 8791–8800. https://doi.org/10.1029/2019GL083619
47. Giuffrida M, Viccaro M, Ottolini L (2018) Ultrafast syn-eruptive degassing and ascent trigger high-energy basic eruptions. *Sci Rep* 8: 147. https://doi.org/10.1038/s41598-017-18580-8
48. Bonadonna C, Ernst GGJ, Sparks RSJ (1998) Thickness variations and volume estimates of tephra fall deposits: the importance of particle Reynolds number. *J Volcanol Geoth Res* 81: 173–187. https://doi.org/10.1016/s0377-0273(98)00007-9
49. Spera FJ (1984) Some Numerical Experiments on the Withdrawal of Magma From Crustal Reservoirs. *J Geophys Res* 89: 8222–8236. https://doi.org/10.1029/JB089iB10p08222
50. Botcharnikov R, Freise M, Holtz F, et al. (2005) Solubility of COH mixtures in natural melts: new experimental data and application range of recent models. *Ann Geophys* 48: 633–646. https://doi.org/10.4401/ag-3224
51. DeNosaquo KR, Smith RB, Lowry AR (2009) Density and lithospheric strength models of the Yellowstone–Snake River Plain volcanic system from gravity and heat flow data. *J Volcanol Geoth Res* 188: 108–127. https://doi.org/10.1016/j.jvolgeores.2009.08.006
52. Jellinek AM, DePaolo DJ (2003) A model for the origin of large silicic magma chambers: precursors of caldera-forming eruptions. *Bull Volcanol* 65: 363–381. https://doi.org/10.1007/s00445-003-0277-y
53. Simakin AG, Ghassemi A (2010) The role of magma chamber-fault interaction in caldera forming eruptions. *Bull Volcanol* 72: 85–101. https://doi.org/10.1007/s00445-009-0306-6
54. Caricchi L, Annen C, Blundy J, et al. (2014) Frequency and magnitude of volcanic eruptions controlled by magma injection and buoyancy. *Nature Geosci* 7: 126–130. https://doi.org/10.1038/ngeo2041